ORIGINAL ARTICLE

David Kibe Muchiri · James N. Hewett · Mathieu Sellier ·
Miguel Moyers-Gonzalez · Jerome Monnier

Numerical simulations of dam-break flows of viscoplastic fluids via shallow water equations

Abstract Abstract This paper presents simulations of dam-break flows of Herschel–Bulkley viscoplastic fluids over complex topographies using the shallow water equations (SWE). In particular, this study aims to assess the effects of rheological parameters: power-law index (n), consistency index (K), and yield stress (τ_c), on flow height and velocity over different topographies. Three practical examples of dam-break flow cases are considered: a dam-break on an inclined flat surface, a dam-break over a non-flat topography, and a dam-break over a wet bed (downstream containing an initial fluid level). The effects of bed slope and depth ratios (the ratio between upstream and downstream fluid levels) on flow behaviour are also analyzed. The numerical results are compared with experimental data from the literature and are found to be in good agreement. Results show that for both dry and wet bed conditions, the fluid front position, peak height, and mean velocity decrease when any of the three rheological parameters are increased. However, based on a parametric sensitivity analysis, the power-law index appears to be the dominant factor in dictating fluid behaviour. Moreover, by increasing the bed slope and/or depth ratio, the wave-frontal position moves further downstream. Furthermore, the presence of an obstacle is observed to cause the formation of an upsurge that moves in the upstream direction, which increases by increasing any of the three rheological parameters. This study is useful for an in-depth understanding of the effects of rheology on catastrophic gravity-driven flows of non-Newtonian fluids (like lava or mud flows) for risk assessment and mitigation.

Keywords Shallow water equations · Viscoplastic · Rheology · Dam-break flows · Sensitivity analysis · Non-flat topography

1 Introduction

Dam-break flows of non-Newtonian fluids such as lava, snow avalanches, debris, and mud flows are commonly observed in nature [1–5]. They are normally generated by the sudden collapse of barricades or reservoirs holding fluids, which results in rapid flows downstream. Unfortunately, the effects of these flows are often catastrophic.

D. K. Muchiri (✉)· J. N. Hewett · M. Selliera
Department of Mechanical Engineering, University of Canterbury, Christchurch, New Zealand
E-mail: david.muchiri@pg.canterbury.ac.nz; davidkibe@aims.ac.za

M. Moyers-Gonzalezb
School of Mathematics and Statistics, University of Canterbury, Christchurch, New Zealand

D. K. Muchiri · J. Monnier
INSA and Institut de Mathématiques de Toulouse (IMT), Toulouse, France

It is thus very important to understand the rheological behaviour and propagation characteristics of dam-break flows for hazard mitigation [6–8].

Previous studies have shown that the propagation of dam-break flows is influenced by various factors, among them, fluid rheological properties, bed slope, topographical variations, and downstream fluid levels, see [9–16] and references therein. These factors play an important role in determining the maximum height and speed of flows downstream. However, for non-Newtonian fluids, in particular viscoplastic fluids, the influence of these factors on dam-break flows is still an open field of research. Viscoplastic flows are flows characterized by a yield stress (τ_c) that results in the formation of two regions within the flow: a plug (unyielded) region and a sheared (yielded) one [2,4,17,18]. The two regions are separated by an interface referred to as a yield surface. By deriving consistent thin-layer solutions, [19] demonstrated that the plug region becomes a pseudo-plug (a weakly sheared layer), and the yield surface becomes a fake yield surface. This resolved the so-called plug paradox on the existence or non-existence of a true plug region [4]. Nevertheless, if the stress is below the yield stress, viscoplastic fluids behave like solids.

The propagation of dam-break flows for non-Newtonian fluids (in particular, viscoplastic) strongly depends on rheological properties such as consistency index (K), yield stress (τ_c), and flow behaviour index (n) [2,14,20,21]. The effects of these properties over a dry bed of a dam-break problem have been reported previously, see [22–24]. However, the case of a wet bed or that of a non-flat topography has yet to be considered.

The effects of bed slopes on dam-break flows over a dry channel have been extensively addressed; see, for instance, [11,12,23,25]. The fluid was observed to move further downstream upon increasing the slope [12]. This is different from the observation made recently in [25] for a wet bed case, where increasing the slope was reported to slow the front position. Nonetheless, more needs to be done to investigate the impact of the slope on non-Newtonian flows over a wet bed. Further, the depth of a downstream fluid has also been shown to affect the free-surface dynamics, see [10,12,26]. Experimental and numerical investigations on these effects of tailwater have been summarized in [12] and references therein. However, this has not been reported exhaustively in the case of non-Newtonian fluids.

Bed variations due to the presence of an obstacle or an irregular topography downstream of a dam are another factor that can influence flow dynamics. Apart from blocking the flow, an irregular topography can result in variations in the flow depth and mean velocity. The presence of an obstacle has been shown to cause the formation of a negative wave traveling in the upstream direction, see [13,27]. Dam-break flows over non-flat topographies have been studied in [13,28,29] for example, see also references therein. However, little attention has been given to investigating the impact of topographical variations on dam-break flows of non-Newtonian fluids.

Gravity-driven flows of non-Newtonian fluids are normally described by rheological models such as power-law, Bingham, and Herschel–Bulkley [1–3,20,30–34]. The Herschel–Bulkley model is commonly used (also used herein) because of its ability to describe many complex fluid behaviors in a non-linear and history-independent manner. Coupling with the full Navier–Stokes equations and the transport equation of free-surface dynamics, the Herschel–Bulkley constitutive law can be used to model dam-break flows of viscoplastic fluids. However, solving these equations simultaneously is computationally expensive and time consuming. To overcome such computational difficulties, reduced models such as the lubrication approximation and the shallow water equations (SWE) are usually employed, see, e.g. [2,19,35–39]. The latter is considered herein.

The shallow water equations are usually derived by depth integration, assuming that the depth is much smaller than the characteristic length (the long-wave assumption). However, only a few SWE models for Herschel–Bulkley fluids exist, see [38,40,41]. The numerical computations of the present study rely on the SWE flow model formally derived in [38]. This model enables us to take into account the variation of basal elevation and basal boundary conditions. Nonetheless, one main drawback of depth-averaged models (like the SWE) is that they are limited to shallow (thin) flow problems. If the long-wave assumption is not satisfied (e.g., during the early phase of many dam-break problems), these models may fail to accurately describe the flow dynamics. For that reason, analysis of the flow patterns at early times of a dam-break resulting from the sudden opening of the dam gate is beyond the scope of this work. In addition, it has been shown that flows of viscoplastic fluids on an incline can stop in finite time when the gravitational forces become equal to the yielding conditions, see [16,21] and references therein. The stopping behaviour leading to the arrested (stationary) state is also beyond the scope of this work.

In particular, this paper focuses on the effects of rheological parameters, bed slopes, downstream fluid levels, and obstacles on the velocity field and free-surface dynamics for dam-break flows of viscopastic fluids like lava and mud flows. Numerical simulations are carried out over a dry, wet, and non-flat bed. In each case, the computed results are first compared with experiments for validation.
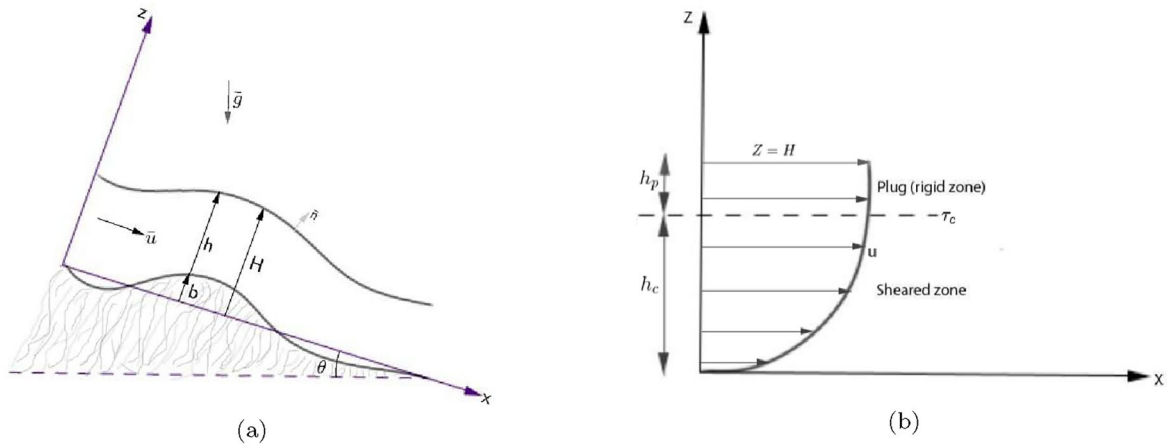
Fig. 1 Sketch showing **a** the flow geometry with a non-flat topography, and **b** the plug and sheared zones in the velocity profile

The outline of the paper is as follows: In Sect. 2, the governing equations and the numerical methods are presented. Section 3 presents the numerical results on dam-break flows for the three different cases considered. In Case 1 (Sect. 3.1), dam-break flows down a dry inclined channel are analyzed. The effects of rheological parameters are discussed in detail. In Case 2 (Sect. 3.2), the numerical results of dam-break flows over a wet channel are discussed. The influence of bed slopes and fluid depth ratios is also analyzed therein. The numerical simulations over a dry non-flat topography are discussed in Case 3 (Sect. 3.3). Conclusions are drawn in Sect. 4.

2 Mathematical formulation

A two-dimensional incompressible flow of a viscoplastic fluid (like lava) down an inclined plane as shown in Fig. 1 is considered, with x being the axis of the slope at an angle θ and z, the axis normal to the slope. The flow is driven by gravity $\boldsymbol{g} = (g\sin\theta, -g\cos\theta)$, and described by its velocity $\boldsymbol{u} = (u, w)$ assuming a hydrostatic pressure field p. The fluid density is denoted by ρ, and the time-dependent fluid depth denoted by $h(t, x, z) = H(t, x, z) - b(x, z)$ where $H(t, x, z)$ is the fluid elevation and $b(x, z)$ the basal topography elevation. The flow is assumed to be independent of the spanwise direction, although a 3D formulation is presented in our previous work [38], which is followed herein.

The governing equations adequate to describe the flow dynamics and rheology of lava are the incompressible Navier–Stokes equations together with the Herschel–Bulkley constitutive law:

Conservation of mass:

$$\partial_x u + \partial_z w = 0 \tag{2.1}$$

Conservation of momentum:

$$\rho(\partial_t u + u\partial_x u + w\partial_z u) = -\partial_x p + \rho g \sin\theta + \partial_x \tau_{xx} + \partial_z \tau_{xz}, \tag{2.2}$$

$$\rho(\partial_t w + u\partial_x w + w\partial_z w) = -\partial_z p - \rho g \cos\theta + \partial_x \tau_{xz} + \partial_z \tau_{zz}. \tag{2.3}$$

The Herschel–Bulkley rheology law is given by

$$\begin{cases} \tau_{xz} = \tau_c + K \left(\partial_z u\right)^n & \text{if } \tau_{xz} > \tau_c \\ \partial_z u = 0 & \text{if } \tau_{xz} \leq \tau_c \end{cases} \tag{2.4}$$

where τ_{xz} is the shear stress, $n > 0$ the power-law index, $K > 0$ the consistency index, and τ_c the yield stress.

The Herschel–Bulkley model provides a good mathematical law from which other fluid models can be obtained. For instance, when $n = 1$, the law reduces to the Bingham model, where the consistency index K becomes the plastic viscosity η. When $n \neq 1$ and $\tau_c = 0$, we have a power-law fluid model. When $n = 1$ and $\tau_c = 0$, the law reduces to a Newtonian fluid model.

The governing equations (2.1)–(2.4), are closed by defining appropriate boundary conditions for the free-surface and the basal topography. For the free-surface at $z = H$, we use the kinematic condition:

$$\partial_t h + u \partial_x H = w \tag{2.5}$$

and the no stress condition: $\left(\underline{\underline{\tau}} - \underline{\underline{I}} p \right) \cdot \hat{n} = 0$ where the unit normal $\hat{n} = \frac{1}{\sqrt{1+(\partial_x H)^2}} \binom{-\partial_x H}{1}$. At the bottom surface, $z = b$, a non-slip condition is used: $u = w = 0$.

The present study relies on the 1D version of the 2D SW model derived in [38]. The derivation is done by depth integration of the above equations applying the long-wave assumption, see Muchiri et al. [38] for the formal asymptotic derivation. The complete model of the SWE in one-dimension reads

$$\partial_t h + \partial_x q = 0,$$
$$\partial_t q + \partial_x \left(\frac{q^2}{h} + \frac{1}{2} g h^2 \cos\theta \right) = gh\cos\theta \, (\tan\theta - \partial_x b) - \frac{1}{\rho} \tau_b, \tag{2.6}$$

with the bottom shear stress approximated as

$$\tau_b = K \left(\frac{K}{\rho g |S_\theta|} \right)^{\frac{1-n}{n}} \left(\frac{\tau_c}{\rho g S_\theta} + h_c \right) \frac{q}{D} \tag{2.7}$$

where S_θ can be taken as $S_\theta = \sin\theta$, a zeroth-order approximation, or as $S_\theta = \sin\theta - \cos\theta \partial_x H$, an enriched approximation with a corrective slope term [38]. It is worth noting that the two approximations give similar results, the difference only appears in areas of sharp changes in the fluid local slopes, as reported in [38]. However, although the former is less expensive to solve, it is not valid for $\theta = 0^o$. The denominator D is given by $D = h_c^{\frac{n+1}{n}} \left[\frac{n}{n+1} h - \frac{n^2}{(n+1)(2n+1)} h_c \right]$, where $h_c(x, t) = \max \left(0, h(x, t) - h_p(x, t) \right)$ is the thickness of the sheared zone, and $h_p(x, t) = \frac{\tau_c}{\rho g S_\theta}$ the plug thickness, see Fig. 1b. The flow rate q is given by $q = h\bar{u} = \int_b^H u \, dz$ where $\bar{u}$ is the mean velocity. We note that the basal shear stress approximation (2.7) is of zeroth order, i.e., the so-called pseudo-plug concept is not considered herein. We also note that this approximation is a development of a similar expression presented in [40]. The difference is how the state variables (h, q) are integrated within the approximation, which makes our model more robust to converge. Furthermore, since dam-break flows in open-channels are dominantly driven by the streamwise pressure gradient, Muchiri et al. [38] propose to further express the gravity source term as $gh\cos\theta\tan\theta \simeq -gh\sec\theta \partial_x h$, where the negative sign indicates the flow direction. This is applied in the following simulations for $\theta > 0^o$.

We also recall the Froude number, $\text{Fr} = \bar{u}/\sqrt{gh \cos\theta}$, the Reynolds number, $\text{Re} = \rho \bar{u}^{2-n} h^n / K$, and the Bingham number, $\text{Bi} = \tau_c h^n / K \bar{u}^n$ from [38], which are calculated herein from the local values, as shown in the next section. The Froude number indicates whether the flow is subcritical (Fr $<$ 1), critical (Fr $=$ 1), or supercritical (Fr $>$ 1), while the Reynolds number indicates whether the flow regime is laminar (Re $<$ 500), turbulent (Re $>$ 2000), or in the transitional range $500 < \text{Re} < 2000$ [42]. The Bingham number, on the other hand, describes the effects of the yield stress relative to the viscous stress. For instance, if Bi $<$ 1, the shear stress exceeds the yield stress, if Bi $>$ 1, the shear stresses are below the yield stress, and if Bi $=$ 0, the flow is Newtonian.

The flow model (2.6)–(2.7) is solved by COMSOL Multiphysics software version 6.0 using the SWE interface, which employs the Finite Element method (a first-order Discontinuous Galerkin scheme in space and Runge–Kutta in time) for discretization of the equations. Each term is matched with the corresponding term in the interface, with the basal shear stress implemented as the domain force. For the numerical computation, we use a uniformly spaced mesh of 3000 elements and a time-step $\Delta t = 0.05$ s, unless stated otherwise.

3 Results and discussion

The model is applied to three dam-break cases discussed in the following sections. In each case, the model is first compared with experiments for validation and to test its applicability (and reliability) to simulate real flows over different geometries. Other simulation results mimicking viscoplastic lava flows are presented and analyzed thereafter. The effects of rheology on the flow depth, velocity, and free-surface profile are investigated and detailed in each case.
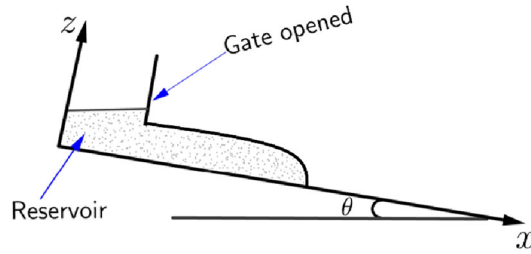
Fig. 2 Side-view sketch of a dam-break problem on an inclined channel

Table 1 Rheological details of Carbopol Ultrez 10 used, data obtained from[11,23]

Concentration (%)	K (Pa s^n)	n	τ_c (Pa)	h_g(m)
0.25	32.1	0.39	78	0.32
0.3	47.7	0.42	89	0.34

3.1 Case 1: Dam-break flows on an inclined flat topography

In this case, we study the influence of rheological parameters on the flow behaviour down an inclined flume. We use data from a dam-break experiment investigated in [11,23], which involves the sudden release of fixed volumes of a viscoplastic fluid down a channel inclined at some angle θ, as shown in Fig. 2. The fluid is initially locked in a reservoir set at the top of the channel before being released suddenly by opening the lock gate to flow freely, driven by gravity, on a dry flat surface.

Following [11], we suppose that the reservoir is of length $l = 0.51$ m, while the channel is of length $L = 6.0$ m, and the inclination angle is $\theta = 12^o$. We impose some initial fluid height defined linearly by $h = h_g + (x - l)\tan\theta$, where h_g is the height at the gate (given in Table 1), and wall boundary conditions on the upstream and downstream walls. The material used for the simulations is 0.3% concentration of Carbopol Ultrez 10 as indicated in Table 1, unless stated otherwise, with density $\rho = 1000$ kg m^{-3}.

The data for simulations and comparison is extracted from[11,23] using WebPlotDigitizer [43], and the figure resolution constraint correspond to an error margin of less than 5%.

The results in Fig. 3 show a good agreement between the experiments and numerical simulations. The slight deviations could be attributed to the experimental uncertainties reported in the literature [11], which are not accounted for in the present model. For instance, besides the dam-wall inertia and some vibrations in the experimental facility, the entire fluid was not released instantly as the gate did not open instantaneously, although the requirement for an instant dam-break is satisfied, i.e., $t \leq \sqrt{2\triangle h/g}$, where $\triangle h$ is the initial difference between the average upstream and downstream fluid levels, see [25] and references therein. On the other hand, for numerical simulations we assumed that upon opening the gate, the entire fluid column was released instantaneously. Therefore, some deviations in the free-surface dynamics between the experiments and simulations are expected.

For the following simulations, the rheological properties of the fluid used are given by Eq. (3.1) and $\left(h_g,\ \theta\right) = (0.34$ m, $12^o)$, unless stated otherwise. Each parameter is varied while keeping other parameters constant.

$$(K,\ n,\ \tau_c) = \left(50\,\text{Pa s}^n,\ 0.6,\ 40\,\text{Pa}\right) \tag{3.1}$$

Figure 4 shows the evolution of the state variables $(h,\bar{u},q)$ at various time instants. As one would expect, the height is observed to reduce in time as the fluid spreads, see Fig. 4a. As shown in Fig. 4b, c, the mean velocity and discharge are at their maximum in early times of dam-break due to the high gradients in fluid height, which reduce in time as the fluid spreads and the available hydrostatic head decreases. Consequently, due to high resistance (e.g., the bottom surface friction), which opposes the x-component of the gravity force, the fluid is observed to decelerate with time.

To determine the flow regime for this set of parameters, the local Froude numbers and Reynolds numbers are plotted over distance for some time instants, as shown in Fig. 5. The Froude numbers indicate that the flow is subcritical. The Reynolds numbers, on the other hand, are very low, showing that the flow is laminar. This is perhaps due to the relatively high values of the rheological parameters used. Consequently, the following simulations in this subsection are assumed to be in the laminar regime. Moreover, these two dimensionless
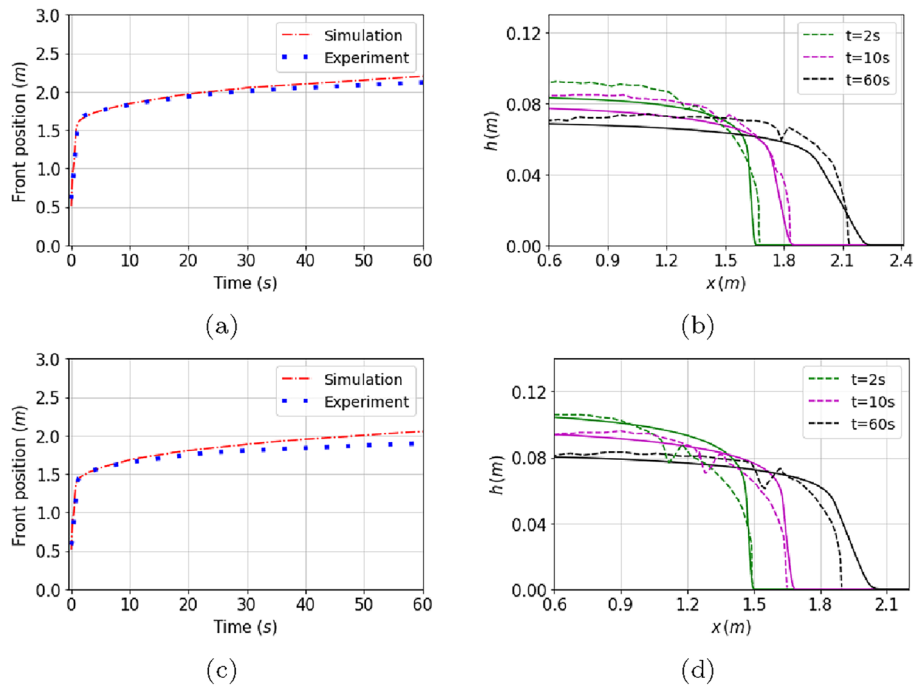
Fig. 3 Comparing front positions (x_f) and free-surface profiles of experiments [11,23] and numerical simulations with time for (**a**) and (**b**) 0.25% and (**c**) and (**d**) 0.3% concentration of Carbopol, respectively. Free-surface profiles of experiments are in dashed lines, and simulations are in solid lines
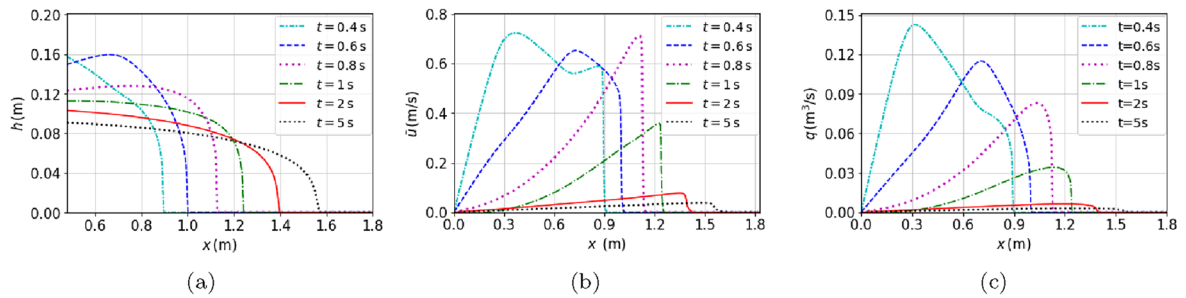

Fig. 4 Time evolution of the **a** fluid height, **b** mean velocity, and **c** flow rate
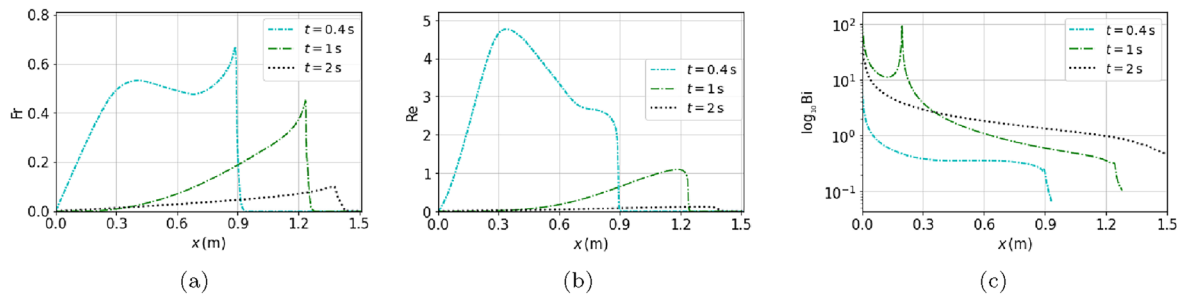

Fig. 5 Variation of **a** Froude, **b** Reynolds, and **c** Bingham numbers over distance at various time instants
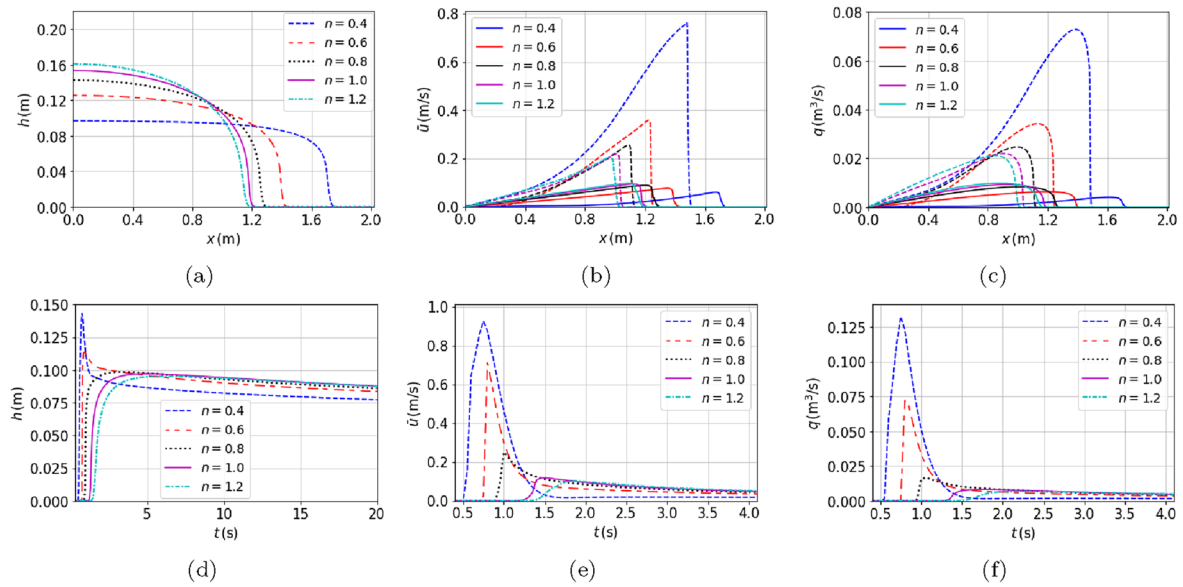
Fig. 6 Effects of flow behaviour index: **a** evolution of the fluid height at $t = 1$ s, the corresponding **b** mean velocity and **c** flow rate at $t = 1$ s (broken line) and $t = 2$ s (solid line), and hydrographs at $x = 1.1$ m for the **d** fluid height, **e** mean velocity, and **f** flow rate, respectively

groups are observed to decrease with time as the flow speed reduces downstream. To determine the strength of the yield stress relative to the viscous stress, the local Bingham numbers are also plotted in Fig. 5 for some time instants. It is observed that at the front position, Bi < 1, while Bi ≥ 1 everywhere else. This indicates that the shear stress exceeds the yield stress at the front positions but is lower than the yield stress everywhere else.

3.1.1 Effects of power-law index

Figure 6 shows the effects of the power-law index on the flow state variables. Increasing the flow behaviour index is observed to slow the progression of the front position, the mean velocity, and the flow rate, as shown in Fig. 6a–c. Evidently, it can be deduced that shear-thickening fluids ($n > 1$) appear to be slower than shear-thinning fluids ($n < 1$). This is due to the increase of the apparent viscosity and hence the friction term, which increases when n is raised, see the rheological law (2.4) and the SWE (2.6). High viscosity slows the dynamics of the flow.

As shown in Fig. 6d, the highest height registered on the hydrograph is reached when n is the smallest. Moreover, maximum heights are reached rapidly within a short time for smaller values of n and gradually for larger values of n. However, after attaining the peak, the height is observed to reduce rapidly within a short period of time for smaller values of n as compared to larger values. The arrival time of the maximum heights is also seen to increase with n. Likewise, it can be observed that the peak velocity and flow rate are registered at early times for smaller values of n, see Fig. 6e, f. Also, the speed and flow rate are observed to reduce rapidly within a short period of time for smaller values of n as compared to larger values of n.

Similar results are shown for the Froude number profiles in Fig. 7, where the Froude numbers decrease with time as the power-law index increases. The flow is supercritical at early times for smaller values of n, after which it transcends to subcritical. For the larger values of n, the flow is generally subcritical. We also note that similar hydrograph results are observed at other positions downstream, away from the dam-gate, see Appendix A.1.

3.1.2 Effects of yield stress

The spreading of the fluid is observed to decrease with increasing yield stress, as shown in Fig. 8. In particular, the free-surface front position, the mean velocity, and the flow rate tend to reduce with time as the yield stress increases, see Fig. 8a–c. Increasing the yield stress increases the friction term, which slows down the fluid
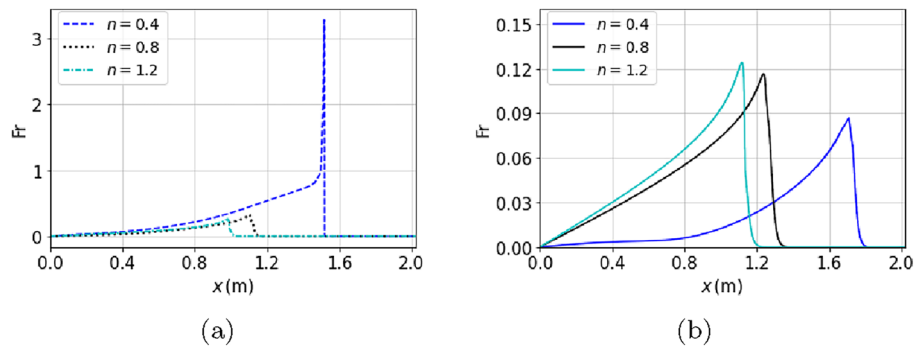
Fig. 7 Variation of Froude numbers over distance for various values of n at **a** $t = 1$ s and **b** $t = 2$ s, respectively
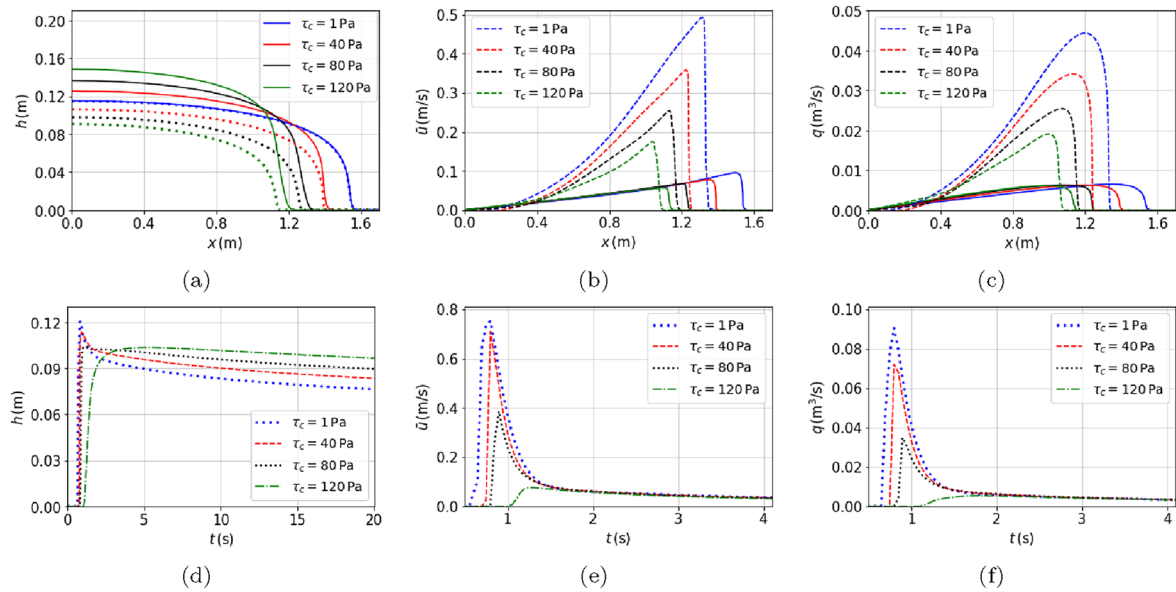

Fig. 8 Yield stress effects: **a** time evolution of the fluid depth and yield surface (broken line) at $t = 2$ s, the corresponding **b** mean velocity, **c** flow rate at $t = 1$ s (broken line) and $t = 2$ s (solid line), respectively, and the respective hydrograph profiles **d**–**f** at $x = 1.1$ m

advancement. Furthermore, the plug thickness (between the yield surface and free-surface) is observed to increase with the yield stress as the yielded zone decreases, see Fig. 8a.

Stage hydrographs in Fig. 8d, show that the fluid thickness increases gradually to reach the maximum heights for the larger values of yield stress and rapidly for the smaller yield stress values. However, the maximum height registered is for the smallest value of yield stress. Also, the rate at which the fluid thickness decreases is smaller for the larger values of yield stress compared to the smaller values. In addition, it can be observed that the arrival time of the maximum elevation is much earlier for smaller yield stresses than for larger values. Likewise, the velocity and flow rate hydrographs register peak values within a short time for the smaller values of yield stress. This clearly depicts that the spreading of the fluid and the maximum height increase by decreasing the yield stress. Moreover, it can also be pointed out that all mean velocity and flow rate curves asymptote to the same value for a long enough time, which indicates that the long-time value is independent of the yield stress value as the entire fluid becomes unyielded with time.

The Froude numbers are also observed to decrease with time as the yield stress increases, see Fig. 9. For smaller τ_c values, the Froude numbers are above unity, hence the flow is supercritical. However, this transcends, with time, to subcritical. For larger τ_c values, the flow regime is entirely subcritical. The Bingham numbers, on the other hand, are larger for larger τ_c values compared to smaller values. This indicates that the yield stresses relative to viscous stresses are larger for larger values of τ_c than for smaller values. The Bingham numbers are also observed to be smaller at the front positions, where the viscous stress is expected to be higher compared to other positions.
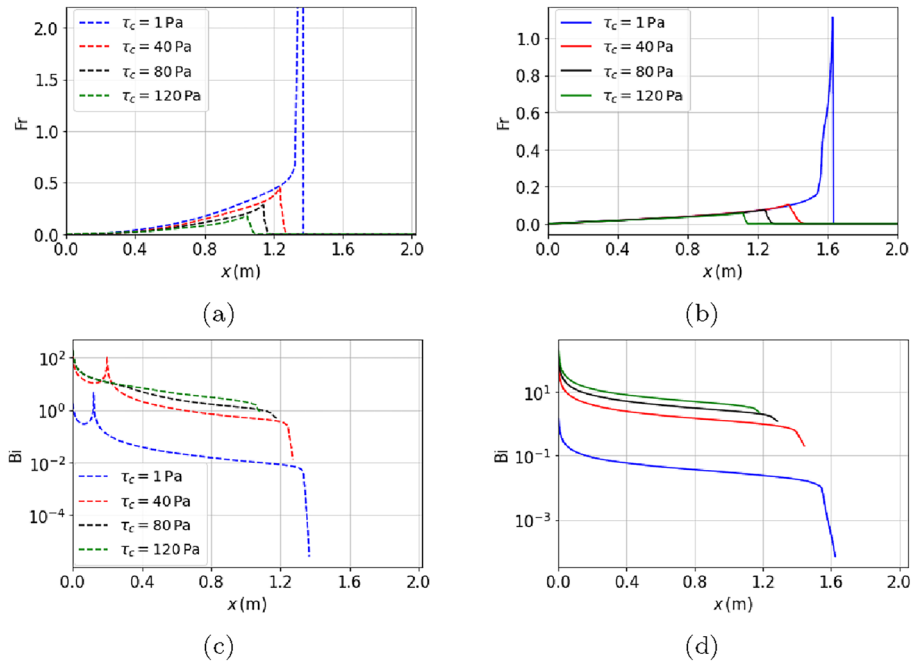
Fig. 9 Variation of **a** and **b** Froude and **c** and **d** Bingham numbers over distance for various values of τ_c at $t = 1$ s and $t = 2$ s, respectively
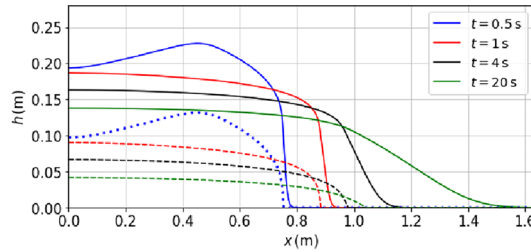

Fig. 10 Yield stress effects: time evolution of the fluid height (solid line) and the corresponding yield surface (broken line) for $\tau_c = 200$ Pa

Figure 10 shows the fluid height profiles and their corresponding yield surfaces for a gravity-induced yield stress ($\tau_c \simeq 200$ Pa), calculated from the relation $\tau_c = \rho g h_p \sin\theta$. It can be observed that as the fluid propagation increases with time, the spreading rate is reducing due to the retardation associated with the basal friction. It can be noticed that the plug thickness for $\tau_c = 200$ Pa is much higher than for smaller τ_c values seen in Fig. 8a, as one would expect, see also Fig. 1b. It can also be observed that the plug thickness at the front position increases with time. This is because the stress at the front position is decreasing as the flow slows down, which indicates that a greater proportion becomes unyielded, see [16].

3.1.3 Effects of consistency index

The front position of the free-surface, the mean velocity, and the discharge are observed to increase with the decrease in consistency index, as shown in Fig. 11a–c. The consistency index increases the apparent viscosity of the fluid, which reduces fluid motion. By comparing the $t = 2$ s and the $t = 1$ s profiles, the mean velocity and the flow rate are observed to reduce with time as the fluid decelerates due to friction. This evidently shows that the state variables (heights, mean velocities, and flow rates) are at their maximum near the gate and decrease with time in the downstream direction.

The fluid elevation is seen to increase gradually over time towards the peak for the larger values of consistency index, see Fig. 11d. For the smaller values of consistency index, the peak is reached rapidly within a short time, though it registers the highest peak. Similarly, for the smaller values of consistency index, the
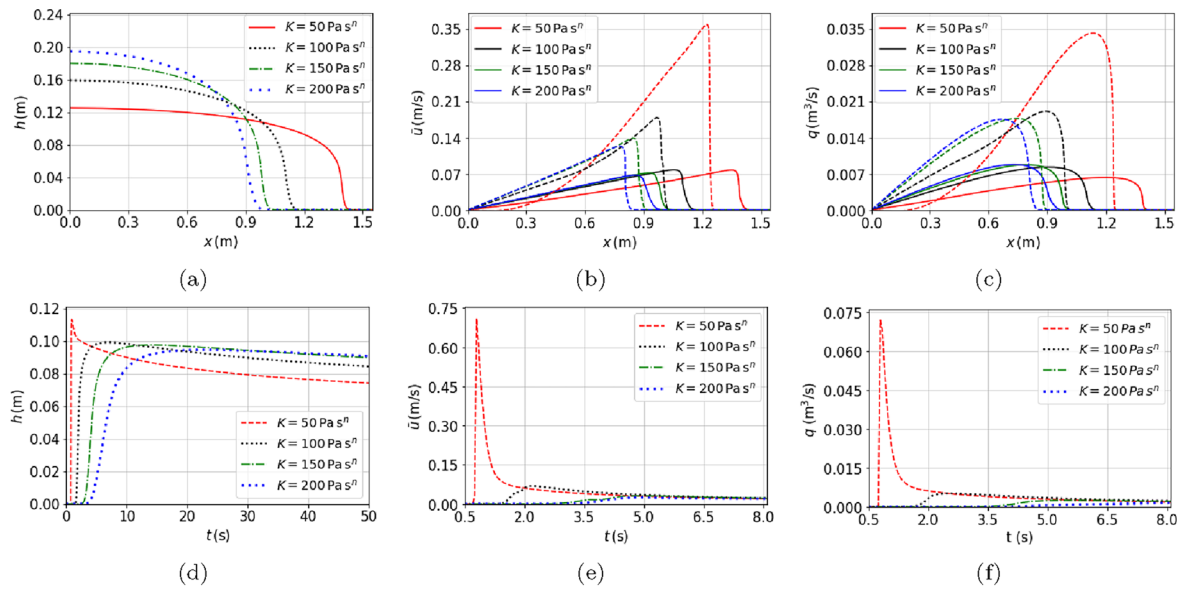
Fig. 11 Effects of consistency index: **a** the fluid depth evolution at $t = 2\,\text{s}$, **b** the corresponding mean velocity and **c** flow rate at $t = 1\,\text{s}$ (broken line) and $t = 2\,\text{s}$ (solid line), respectively, **d**–**f** stage, velocity and discharge hydrographs, respectively, at $x = 1.1\,\text{m}$

mean velocity and the flow rate are observed to shoot within a short period of time compared to the larger values, see Fig. 11e, f. In addition, the arrival time of the maximum values is much earlier for the smaller K values as compared to the larger values. A high consistency index corresponds to high viscosity, which leads to slow motion. Based on the previous results (see, e.g., Fig. 5), the Froude numbers for these K values are expected to be below unity, hence the flow regimes are subcritical.

3.1.4 Flow response for various fluid types

Figure 12 shows the flow response for different types of rheologies under the same geometric conditions: the power-law fluid is obtained by setting $\tau_c = 0\,\text{Pa}$ and $n = 0.6$, the Herschel–Bulkley fluid ($\tau_c = 40\,\text{Pa}$, $n = 0.6$), the Newtonian fluid ($\tau_c = 0\,\text{Pa}$, $n = 1$), and the Bingham fluid ($\tau_c = 40\,\text{Pa}$, $n = 1$). The consistency index, $K = 50\,\text{Pa}\,\text{s}^n$, is kept the same for all the fluid types. The power-law fluid is observed to advance faster than the Herschel–Bulkley, Newtonian, and Bingham fluids in that order, see Fig. 12a. The corresponding mean velocity and flow rate profiles appear to have different flow responses for different fluids, see Fig. 12b, c, respectively. By analyzing the $t = 1\,\text{s}$ and $t = 2\,\text{s}$ profiles, it can be observed that the power-law and Herschel–Bulkley fluids tend to have a similar flow response that is different from that of Newtonian and Bingham fluids.

This difference increases as the power-law index for power-law and Herschel–Bulkley fluids reduces, see also Fig. 6. In addition, it can be observed that the Herschel–Bulkley fluid tends to lag behind the power-law fluid and the Bingham fluid behind the Newtonian fluid. This is due to the effect of yield stress, which is absent in power-law and Newtonian fluids.

At $t = 1\,\text{s}$, the power-law fluid records the highest values of the mean velocity, while the Bingham fluid records the lowest peak. However, at $t = 2\,\text{s}$, we start observing the opposite; the Bingham fluid registering the highest mean velocity and discharge. This is clearly depicted in the hydrographs in Fig. 12e, f, where the mean velocity and the discharge of power-law and Herschel–Bulkley fluids increase rapidly to the peak and then fall rapidly to minimum velocities. For Newtonian and Bingham fluids, the peak is reached gradually with time and remains highest over time. However, the power-law and Herschel–Bulkley fluid register maximum values within a short period of time.

Likewise, the power-law (then the Herschel–Bulkley) fluid registers a maximum height within a short period of time. However, the height of the Herschel–Bulkley fluid does not decrease rapidly as compared to that of the power-law fluid. Again, this is due to the influence of the yield stress in Herschel–Bulkley fluids, which is absent in power-law fluids. Moreover, the heights of Newtonian and Bingham fluids grow gradually with time, with the Bingham fluid remaining thickest over a long time. A zero yield stress plus a smaller value
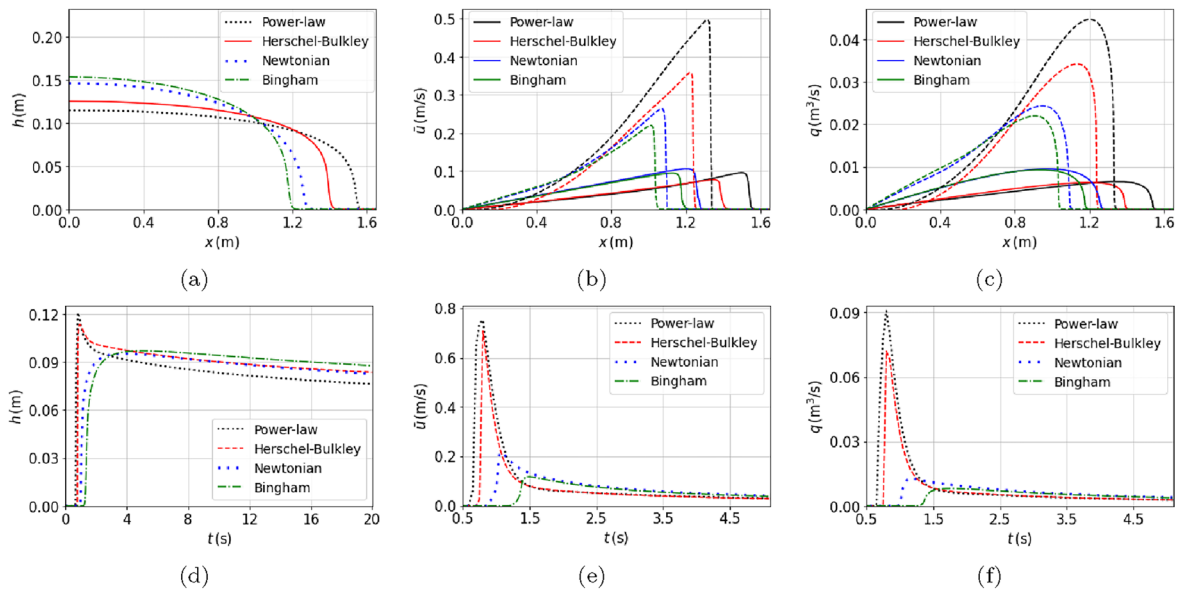
Fig. 12 Flow response of different fluid types: **a** fluid depth profiles at $t = 2$ s, **b–c** the corresponding mean velocity and flow rate profiles at $t = 1$ s (broken line) and $t = 2$ s (solid line), respectively, **d–f** hydrographs at $x = 1.1$ m for the fluid height, mean velocity and flow rate, respectively
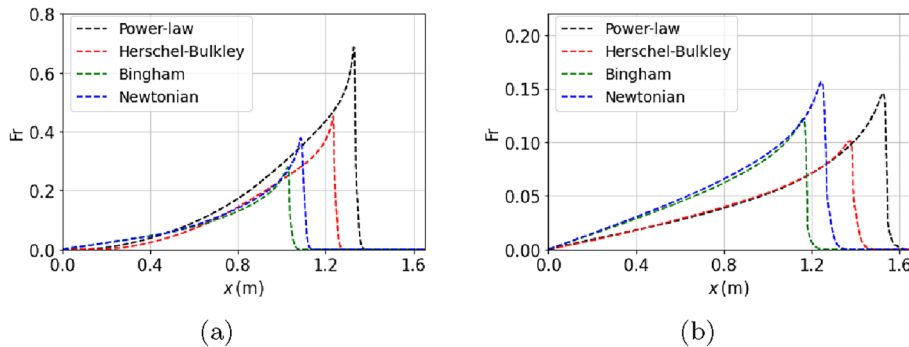

Fig. 13 Variation of Froude numbers over distance for the four fluid types at **a** $t = 1$ s and **b** $t = 2$ s, respectively

of the flow-behaviour index in the power-law fluid makes it spread rapidly compared to others within a short period of time.

Furthermore, the Froude numbers for the four types of fluids are below unity, see Fig. 13, indicating that the flows are subcritical. For the present sets of rheological parameters, the flow is also laminar, as we had seen earlier. It is worth noting that we observe similar results (not shown here) at other positions in the downstream, as shown previously in Fig. 28 in Appendix A.1.

3.1.5 Sensitivity analysis

To determine the contribution of each rheological parameter to the flow behaviour, based on a sensitivity analysis, the front positions for various values of each parameter are plotted for comparison, as shown in Fig. 14. The range of values was chosen from a reference point ($K = 50$ Pa s^n, $n = 0.6$, $\tau_c = 40$ Pa), see Eq. (3.1), such that each rheological parameter changes by a factor of 2. That is; $K = [25$ Pa s^n, 200 Pa s$^n]$, $n = [0.3, 2.4]$, and $\tau_c = [20$ Pa, 160 Pa$]$. The data is normalized so that its variation falls between zero and one for the three parameters. This is achieved using the expression $y_{norm} = \frac{y - y_{min}}{y_{max} - y_{min}}$, where y is the actual value of the rheological parameter and y_{norm} is the corresponding normalized value. The maximum and minimum values within the range are denoted by y_{min} and y_{max}, respectively. It can be observed from Fig. 14, that decreasing any of the three parameters increases the advancement of the front position, which is in agreement
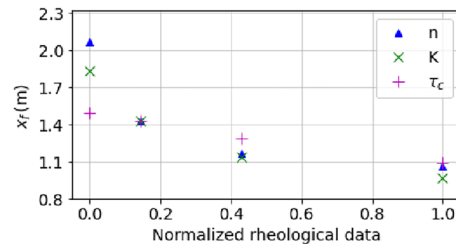
Fig. 14 Effects of the rheological parameters (n, K, τ_c) on the fluid response: front positions (x_f) at $t = 2$ s
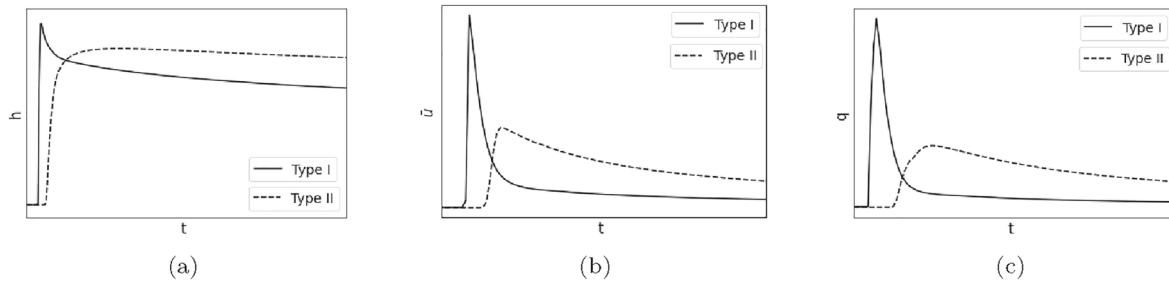

Fig. 15 Types of hydrographs for the **a** free-surface elevation, **b** mean velocity and **c** discharge. Type I and II characterizes flows with a rapid peak and a gradual peak, respectively

with the previous observations. However, by comparing the slopes, the power-law index appears to have more effects on the fluid response, when compared to the other parameters.

3.1.6 Types of hydrographs

Hydrographs are often used to monitor how flows change over time and can be used for the prediction and management of risks [6,44,45]. By studying the shape and size of a hydrograph, one can make predictions about the timing, intensity, and severity of flows. Although hydrographs have different shapes and sizes, we can define two major (extreme) types of hydrographs for dam-break flows discussed so far, arising from the influence of rheological parameters, as shown in Fig. 15:

  i Type I: flows with a rapid peak
  ii Type II: flows with a gradual peak

In Type I, the flow thickness increases rapidly to the peak within a very short time, after which it starts decreasing rapidly with time. In Type II, the flow reaches the maximum elevation gradually over time before decreasing slowly compared to Type I, see Fig. 15a. Similarly, the mean velocity for Type I shoots within a short period of time before decreasing rapidly with time. This is opposite for Type II, in which the mean velocity grows gradually to the peak before it starts reducing, see Fig. 15b. The discharge hydrograph in Fig. 15c is a reflection of the mean velocity and the height, showing similar trends: a rapid and gradual increase of the flow rate to the peak with time for Types I and II, respectively.

Another difference between the two types is the time of arrival of the wave at the hydrograph position. Type I arrives earlier than Type II as seen in the three state variables in Fig. 15. Basically, Type I characterizes flows with relatively high Froude numbers (supercritical), especially during the early stages of a dam-break, before transcending to subcritical over time, while Type II represents relatively slow flows with low Froude numbers (subcritical). Smaller values of n, K, and τ_c are observed to produce Type I hydrographs, while larger values of these parameters produce Type II.

However, very near the dam-gate, where waves are rapid due to the sudden opening of the gate, Type I hydrographs are likely to be observed even for some larger values of rheological parameters. Similarly, far from the gate, where waves are much slower, Type II hydrographs are likely to form even for the lower values of rheological parameters. Similar observations are reported in [25] for Newtonian flows. It is worth noting that there could be other factors that can influence the type of hydrograph, including the bed slope and the volume of the released fluid.
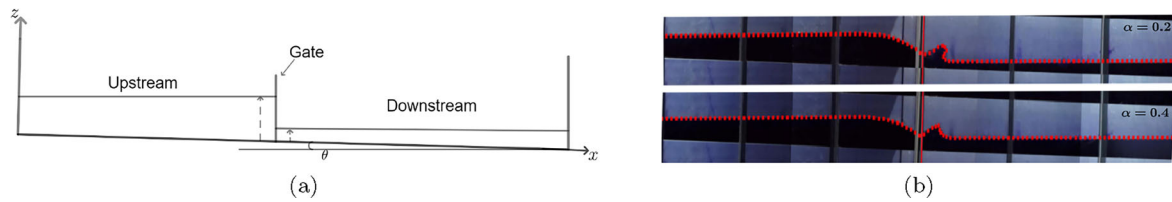
Fig. 16 Dam-break flow over a wet bed: **a** sketch of the problem, **b** screenshot of the experimental results at $t = 0.4$ s for a Newtonian fluid [12]
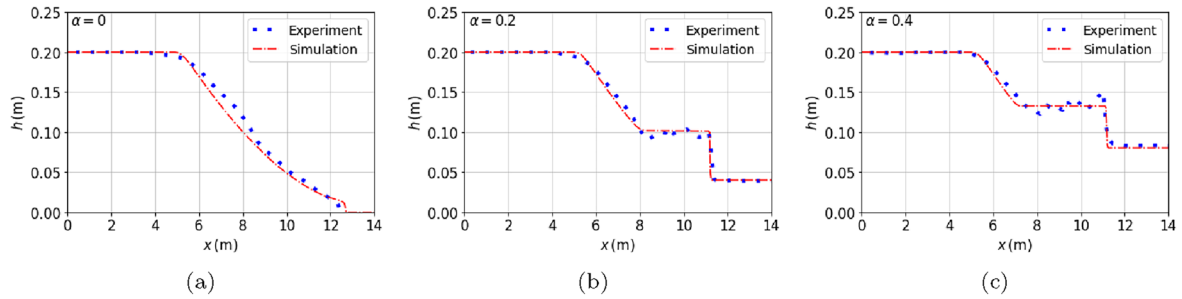

Fig. 17 Comparison of free-surface profiles between experiments and simulation for **a** $\alpha = 0$, **b** $\alpha = 0.2$, and **c** $\alpha = 0.4$ at $t = 1.5$ s

3.2 Case 2: Dam-break flows over an inclined wet bed

In this section, we investigate the effect of rheology on the flow dynamics of a dam-break configuration over a wet bed. Numerical results are compared with experimental data from [12,25]. An experimental setup described in [12] is considered for validation purposes, where the flume is 18 m in length and the bed slope is 0.02, see Fig. 16. A reservoir gate of thickness 1.5 cm, is located 8.37 m from the upstream wall to separate the upstream and the downstream regions. We assume a fixed wall at the downstream end.

For the upstream, an initial fluid height of 0.2 m is used. For the downstream, three initial fluid depths of 0.0 m, 0.04 m, and 0.08 m are considered, giving the following depth ratios: $\alpha = 0$, $\alpha = 0.2$, and $\alpha = 0.4$, respectively. To compare with experiments, numerical simulations are carried out using a Newtonian fluid obtained by setting the rheological parameters as in Eq. (3.2). A uniformly spaced mesh of 3000 elements is used here for computation.

$$(K, \ n, \ \tau_c) = \left(0.01 \, \text{Pa s}^n, \ 1, \ 0 \, \text{Pa}\right) \tag{3.2}$$

As shown in Fig. 17, there is a good agreement between the experiments and simulations. It is observed that the fluid travels a longer distance on a dry surface ($\alpha = 0$), as compared to cases of a wet surface within the same duration. Moreover, for a wet bed, the progression of the front position is observed to decrease when the tail-fluid is increased, as shown for $\alpha = 0.2$ and $\alpha = 0.4$ in Fig. 17b, c, respectively. As the depth ratio increases, the hydrostatic head that drives the flow reduces, which slows fluid propagation, making the wave front position tend to decrease. The front position in this case is defined as the location where the free-surface reaches the downstream asymptotic value.

The jet-like rising of the fluid surface at early dam-break stages reported in the literature [12,25,46], see Fig. 16b, is also observed numerically, though not well predicted (not shown here), as the flow from the reservoir interacts with the downstream static fluid. The rising height for $\alpha = 0.2$ is observed to be higher than that for $\alpha = 0.4$, which is in agreement with experimental results.

To consider a real-like viscoplastic flow, e.g., a less viscous lava [9,15,47,48], a Herschel–Bulkley case is considered with the rheological parameters given by Eq. (3.3) and increasing the slope angle to $\theta = 6^o$, unless stated otherwise.

$$(K, \ n, \ \tau_c) = \left(10 \, \text{Pa s}^n, \ 0.6, \ 10 \, \text{Pa}\right) \tag{3.3}$$

Firstly, we determine the flow regime for $K = 10$ Pa s (Newtonian) with respect to the experimental one, of $K = 0.01$ Pa s, by plotting the Froude and Reynolds number hydrographs for various depth ratios, as shown in Fig. 18.

For $K = 0.01$ Pa s, the flows are observed to be supercritical and turbulent, at least for $\alpha = 0$ and $\alpha = 0.2$, see Fig. 18a, b. For $\alpha = 0.4$, the Froude numbers are below unity, hence subcritical but still turbulent, as shown
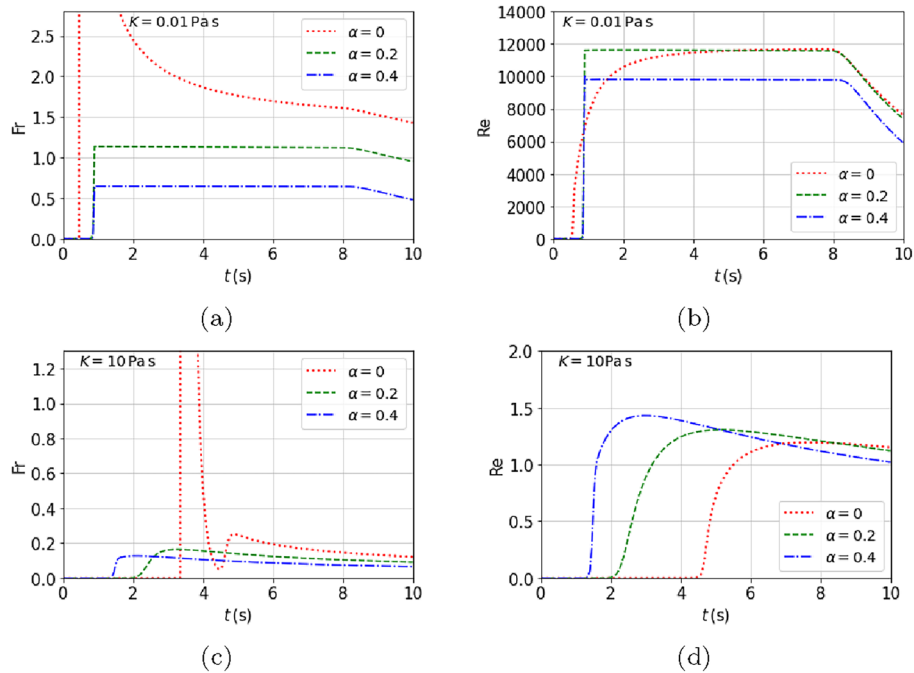
Fig. 18 Froude and Reynolds number hydrographs at $x = 10$ m for Newtonian flows with **a** and **b** $K = 0.01$ Pa s, and **c** and **d** $K = 10$ Pa s for the three depth ratios, respectively

in Fig. 18b. For $K = 10$ Pa s, the flow is supercritical for $\alpha = 0$ and subcritical for $\alpha = 0.2$ and $\alpha = 0.4$, but all are in the laminar regime, see Fig. 18c, d, respectively. It is evident that the Froude and Reynolds numbers decrease with the increase in consistency index, as had been seen in the previous subsection.

Moreover, for the two cases, the peak values of the two numbers are observed to decrease with the increase in depth ratio. This is due to the decrease in velocity as the depth ratio increases. However, the time where the peak values are first registered is observed to decrease with the increase in depth ratio for $K = 0.01$ Pa s (in agreement with experiments in Fig. 17) and to increase with the increase in depth ratio for $K = 10$ Pa s. Increasing the viscosity (consistency index) decreases the interaction between the upstream and downstream fluids, which lowers the impact force (due to the upstream fluid) at the interface between the two fluids, thus reducing the viscous dissipation rate. This makes the upstream fluid layer tend to speed up as the depth ratio increases for $K = 10$ Pa s.

3.2.1 Flow response of different fluid types

Contrary to the previous observation for $K < 1$ Pa s^n (Re > 2000) in Fig. 17, the effects of a wet bed for $K = 10$ Pa s^n (Re < 500) are observed to increase the front position downstream for all fluid types, see Fig. 19. As explained above, increasing the consistency index lowers the Reynolds number, which means that the interaction between the upstream and downstream fluids is reduced (the flow is less vigorous), which lowers the viscous dissipation rate. This explains why the progression of the front position tends to increase when the K value is raised. The interaction between the two fluids reduces further by increasing the fluid depth ratio, thereby increasing the front position advancement, as seen in Fig. 19a–c.

For all three depth ratios, the power-law fluids are observed to spread furthest, followed by Herschel–Bulkley, Newtonian, and Bingham fluids in that order, under the same conditions. This is largely due to the influence of the power-law index, which is higher for Newtonian and Bingham fluids than for power-law and Herschel–Bulkley fluids. Increasing the power-law index increases the friction term and hence slows down the fluid motion, see Eq. (2.7). Moreover, the peak thicknesses of Herschel–Bulkley and power-law fluids are observed to be higher than those of Newtonian and Bingham fluids in that order, as shown in the stage hydrographs in Fig. 19g–i. The peak height of Herschel–Bulkley is higher than that of power-law (and that of Bingham is higher than that of Newtonian) fluids due to the effect of the yield stress, which is absent in
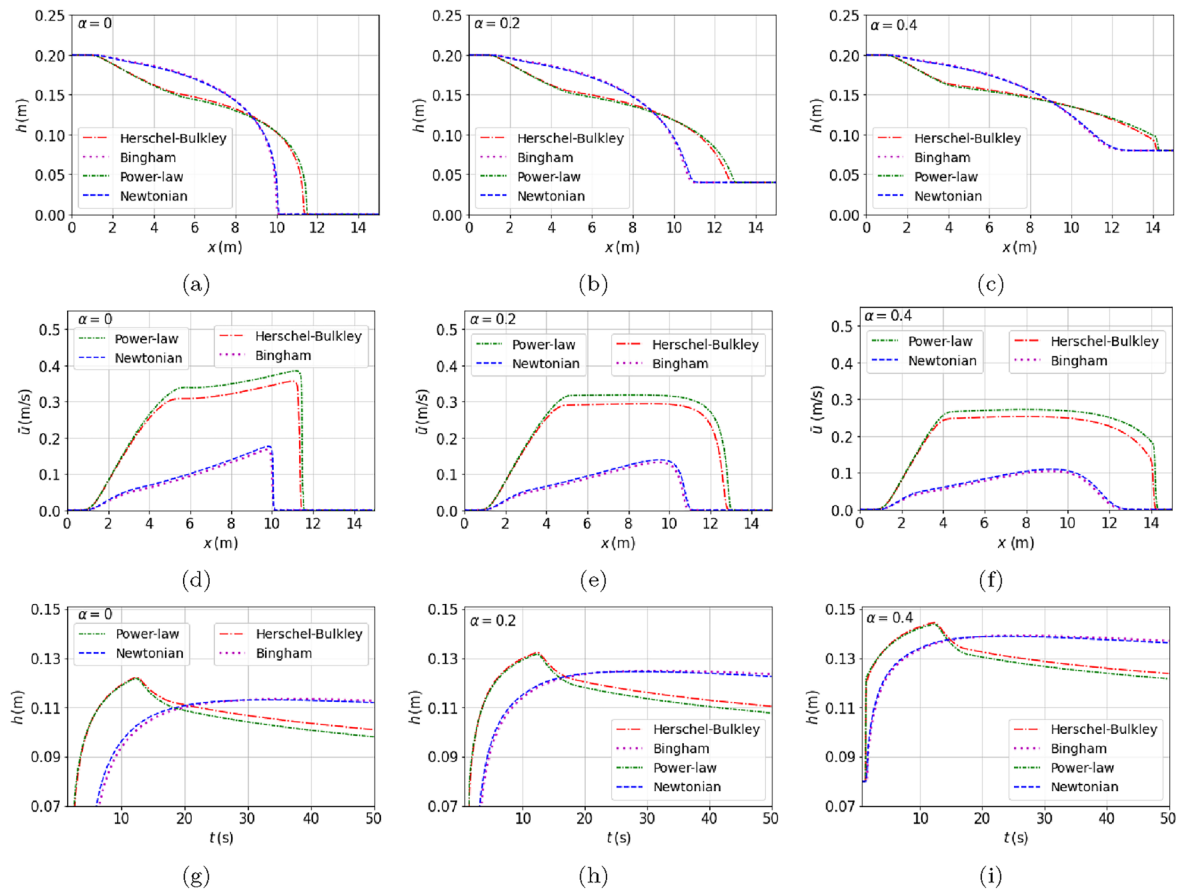
Fig. 19 Flow response of different fluid types: comparison of free-surface profiles (**a**)–(**c**), mean velocity (**d**)–(**f**) at $t = 5$ s, and stage hydrographs at $x = 10$ m (**g**)–(**i**), for $\alpha = 0$, $\alpha = 0.2$, and $\alpha = 0.4$, respectively

power-law (and Newtonian) fluids. Moreover, the free-surface elevation increases with increasing the depth ratio as the volume of the fluid in the flume increases.

Moreover, the mean velocity of power-law fluids is observed to be higher than that of Herschel–Bulkley, Newtonian, and Bingham fluids in that order, see Fig. 19d–f. Again, this is mainly due to the influence of the flow-behaviour index, as explained earlier. However, the peak velocity is observed to reduce with increasing the depth ratio for the four fluid types. Increasing the downstream fluid reduces the thickness of the moving layer, which implies a decrease in the gradient of the fluid height which plays a big part in fluid evolution. The shape of the velocity profile at the front position for $\alpha = 0$ indicates the effects of the bottom friction, which appear low for other ratios. For non-zero depth ratios, the wave front positions tend to speed up over a low-friction surface, with the spreading increasing with the depth ratio.

As seen previously, it is observed that power-law and Herschel–Bulkley fluids appear to have a similar flow response that is different from that of Newtonian and Bingham fluids, see Fig. 19. Both power-law and Herschel–Bulkley fluids attain their maximum heights within a short time, unlike Newtonian and Bingham fluids, for which the heights tend to grow gradually with time before reaching the peak. The arrival time of the maximum height at the hydrograph position is also different for different fluid types. For the power-law and Herschel–Bulkley, the arrival time is much earlier than that of Newtonian and Bingham fluids. This difference is observed to increase or decrease as the power-law index approaches zero or unity, respectively, see also Fig. 21. This indicates that the power-law index is the dominant factor in dictating the fluid response.

3.2.2 Effects of bed slope

Figure 20 shows the effects of bed slopes on the fluid evolution for different depth ratios. As shown in both dry and wet bed cases in Fig 20a–c, the wave front position moves further downstream with increasing bed slope.
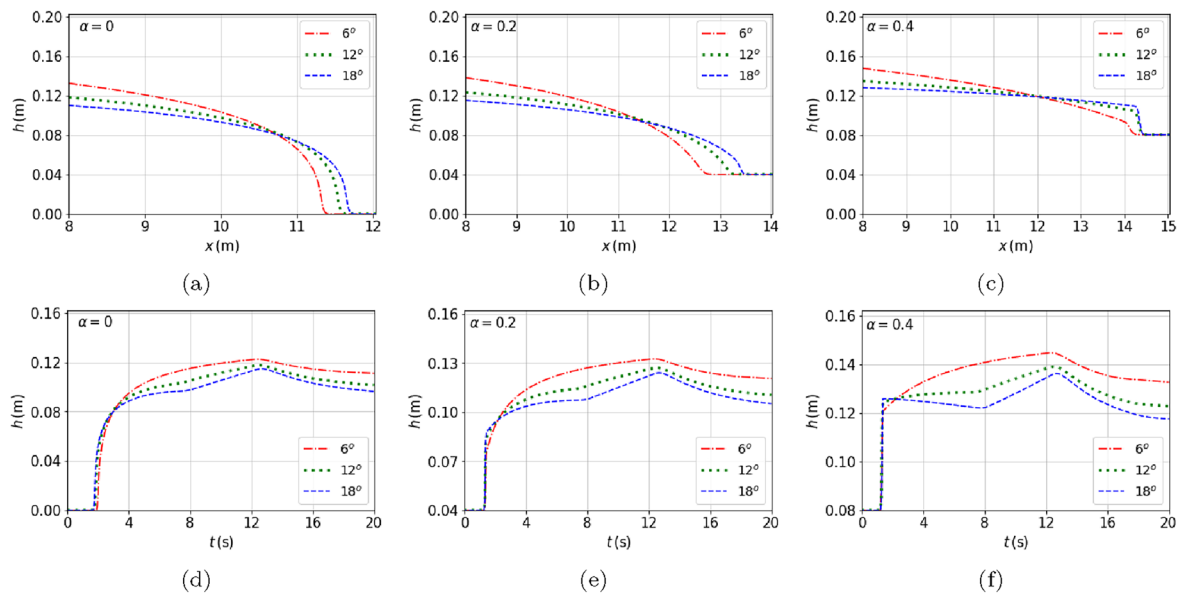
Fig. 20 Effects of bed slopes: **a–c** free-surface profiles at $t = 5$ s and **d–f** the corresponding stage hydrographs at $x = 10$ m, for the three depth ratios: $\alpha = 0$, $\alpha = 0.2$, and $\alpha = 0.4$, respectively

Increasing the slope increases the x- component of acceleration due to gravity. For a wet bed, the front position tends to travel further with the increase of the slope and/or the depth ratio. Increasing the slope or the depth ratio increases the fluid in the downstream, which lowers the gradient of the upstream fluid, thereby minimizing the interaction between the upstream and downstream fluids. Consequently, the spreading top-layer tends to move faster with the increase in bed slope and depth ratio. Moreover, the free-surface elevation increases with the slope as the fluid level increases downstream.

This is contrary to the observations made previously in Fig. 17 (and in the literature [12,25]) for Newtonian flows with a viscosity of water, $K \approx 0.001$ Pa s, where the increase of the bed slope increases the fluid depth in the downstream region, which increases the blockage effects, hence more energy dissipation, making the front position progression tend to decrease.

3.2.3 Effects of rheological parameters

The effects of the three rheological parameters (K, n, and τ_c) for $\alpha = 0.2$ are shown in Fig. 21. It can be observed that the free-surface front position, maximum height, and mean velocity increase with the decrease in power-law index, see Fig. 21a–c. As explained earlier, reducing the power-law index reduces the apparent viscosity and the friction term, hence increasing the fluid flow dynamics.

Decreasing the consistency index is also observed to increase the front position, the maximum height, and the mean velocity, see Fig. 21d–f. Reducing the consistency index implies a decrease in viscosity which increases the fluid propagation. A high consistency index increases the resistance to fluid motion, causing a decrease in fluid evolution.

Similarly, the front position and the mean velocity are observed to increase by reducing the yield stress, as shown in Fig. 21g, i. Increasing the yield stress increases the basal friction term, which slows down fluid propagation. However, the fluid thickness increases with increasing yield stress. We also note that the maximum height is reached gradually or rapidly by increasing or decreasing any of the three parameters, respectively.

3.3 Case 3: Dam-break flows over a non-flat topography

In this section, we study the effects of rheological parameters on the flow behaviour over an obstacle. We consider the set–up of a dam-break flow over a bump on a horizontal channel as presented in [13], and shown in Fig. 22. The channel is of length 8.9 m and height 0.34 m. The reservoir located 4.65 m from the channel
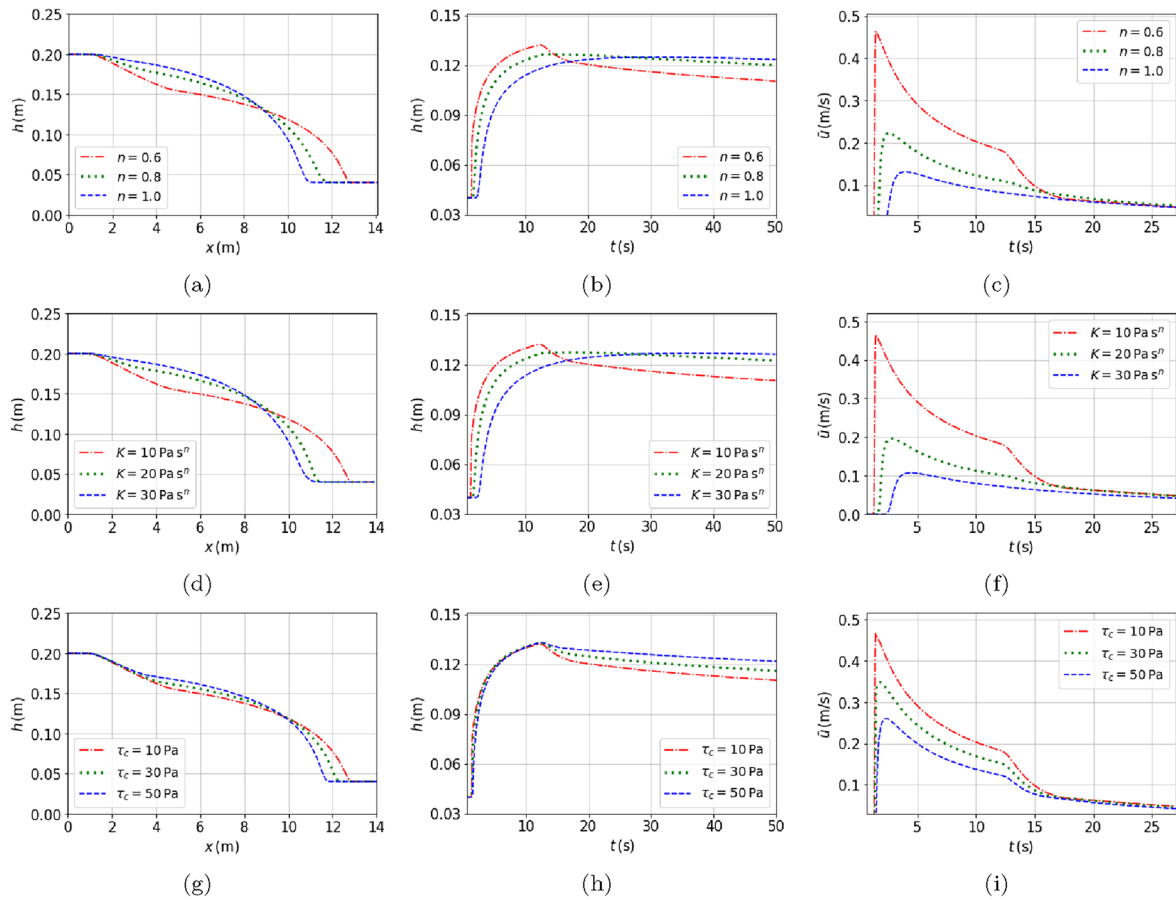
Fig. 21 Effects of parameters n, K and τ_c for $\alpha = 0.2$: (left) free-surface profiles at $t = 5\,\text{s}$, (center) stage hydrographs, and (right) velocity hydrographs at $x = 10\,\text{m}$
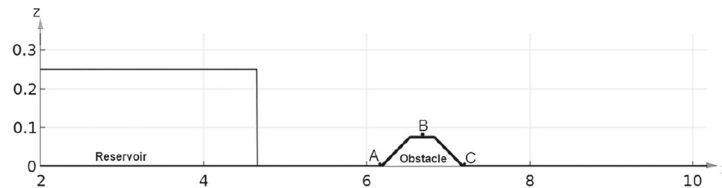

Fig. 22 Sketch of a dam-break problem on a dry surface with a bump (not to scale)

entrance is initially filled with water of height 0.25 m. A trapezoidal shaped obstacle of height 0.075 m, base length 1 m, and top length 0.3 m, is located 6.18 m downstream from the entrance.

The fluid was released suddenly from the reservoir to flow past the obstacle, while the flow behaviour was recorded with video cameras [13]. Numerical results for a Newtonian fluid with a consistency index equivalent to that of water $K = 0.001\,\text{Pa}\,\text{s}$, are compared with the experimental results in Fig. 23. Other rheological parameters used are given by Eq. (3.2), and with the fluid density $\rho = 1000\,\text{kg}\,\text{m}^{-3}$. The free-surface profiles are compared for different time instances: 1.9 s (a), 3.35 s (b), and 4.7 s (c), over the obstacle.

An upsurge of the fluid is observed to develop around the obstacle, see Fig. 23. The surge grows in the upstream direction with time behind the obstacle as the rest of the fluid flows downstream. The surge formation is due to the reflection of the flow wave against the obstacle [13]. There is a good agreement between the experimental results and the numerical results. A slight deviation of the numerical prediction relative to the experimental observations on the reflected wave is observed at $t = 4.7\,\text{s}$, otherwise, the front of the surge is well predicted.

(a) $t = 1.9\,\text{s}$ (b) $t = 3.25\,\text{s}$ (c) $t = 4.7\,\text{s}$
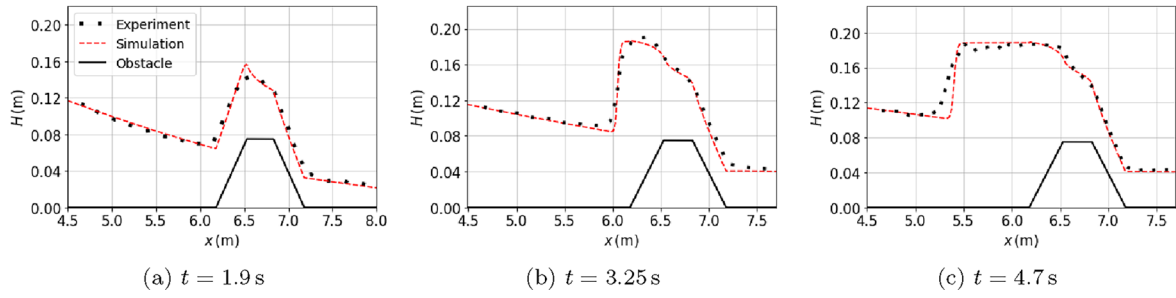
Fig. 23 Comparison between experimental data [13] and simulations using a Newtonian fluid ($K = 0.001\,\text{Pa s}$, $n = 1$, $\tau_c = 0\,\text{Pa}$)
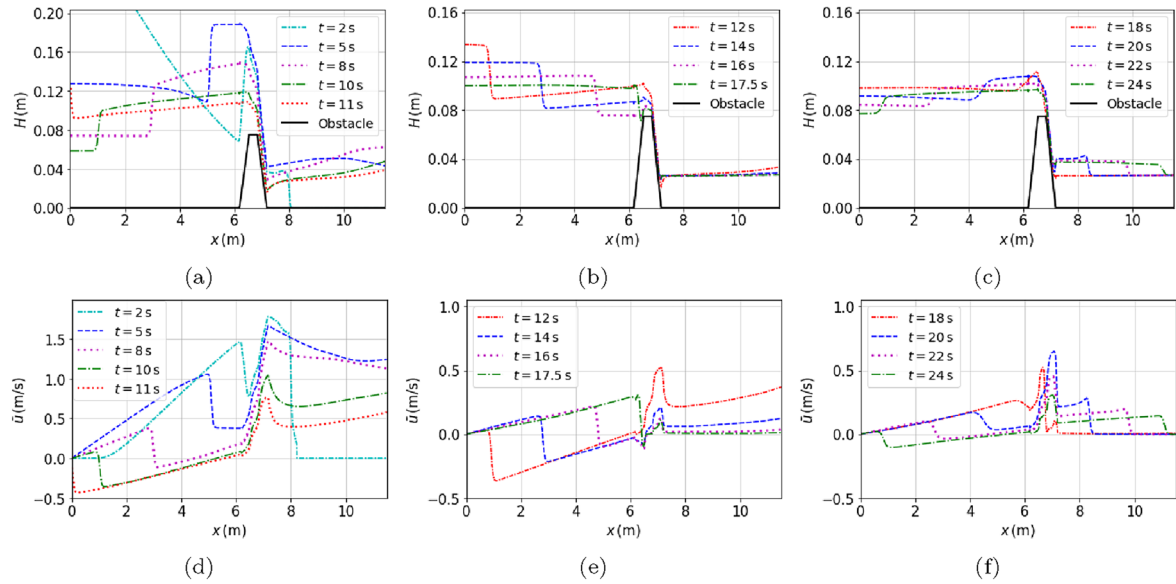

Fig. 24 Development of the surge with time: **a**–**c** surface elevations and the corresponding mean velocities (**d**)–(**f**)

For the following simulations in this section, we consider a relatively more viscous Herschel–Bulkley fluid (e.g., a less viscous lava) with $K = 1\,\text{Pa s}^n$ (other rheological parameters used are given by Eq. (3.4)) and on a slope of $\theta = 6^o$ [9,47,48], unless stated otherwise.

$$(K, \ n, \ \tau_c) = \left(1\,\text{Pa s}^n, \ 0.6, \ 0.4\,\text{Pa}\right) \tag{3.4}$$

3.3.1 Blockage effects of an obstacle

Figure 24 shows the development of the surge with time into negative and positive waves (propagating in the negative and positive directions, respectively). The presence of an obstacle causes the formation of an upsurge in the upstream direction of the obstacle, which is observed to grow in height towards a maximum height around $t = 5$, see Fig. 24a. After attaining its peak height, it starts moving backward on the free-surface as its height reduces. This forms the first negative wave in the upstream direction. On reaching the upstream wall around $t = 11\,\text{s}$, this wave is reflected in the downstream direction, forming a second positive wave, see Fig. 24b. This wave is seen to propagate as it reduces in size. Due to the interference of the obstacle, a second upsurge is observed to start forming around $t = 17.5\,\text{s}$, which develops into a second negative wave that moves again in the upstream direction, see Fig. 24c. At the same time, the second positive wave continues moving past the obstacle in the downstream direction on the free-surface of the first wave.

This phenomenon is observed to repeat itself, forming a series of positive and negative waves behind the obstacle until no more fluid can flow past the obstacle. Correspondingly, a series of positive waves that build upon each other are also observed past the obstacle, see Fig. 24c. This increases the fluid elevation with time on the downstream side until no more fluid is able to be transferred from the upstream, limited by the height of
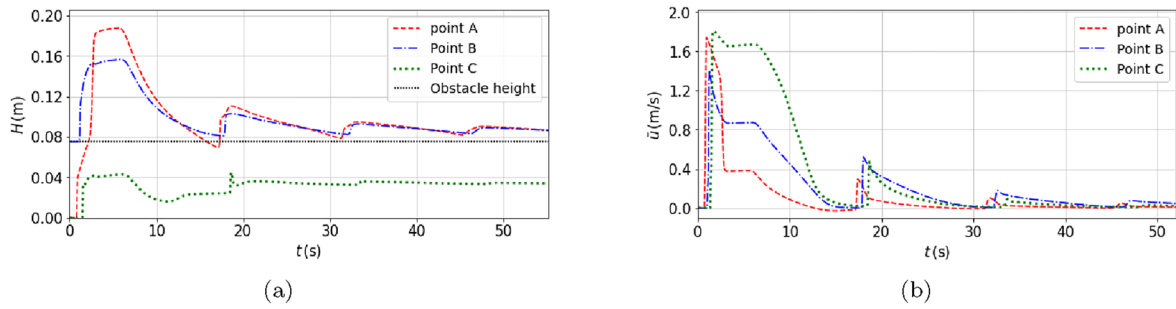
Fig. 25 Hydrographs for the **a** surface elevation and **b** corresponding mean velocity at Point A, B and C
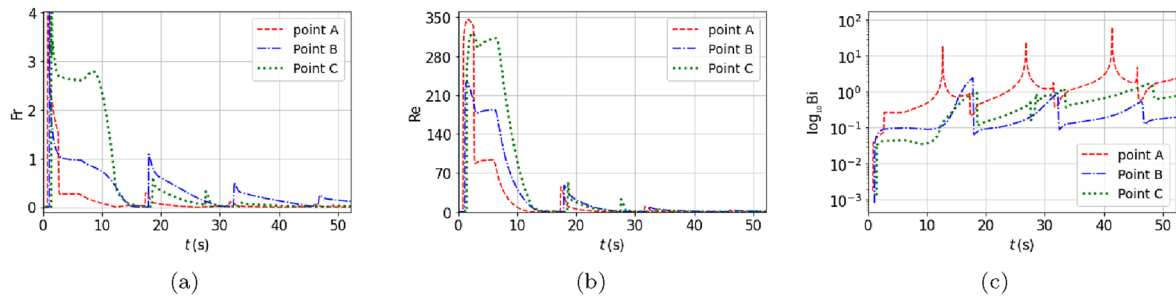

Fig. 26 Hydrographs for the local **a** Froude, **b** Reynolds, and **c** Bingham numbers at Point A, B, and C

the obstacle. The amplitudes (heights) of the waves, measured from the free-surface, reduce one after the other as the fluid evolves. This is as the total fluid elevation reduces in the upstream direction of the obstacle and increases downstream of the obstacle. We also note some shocks right behind the obstacle due to its blockage.

The mean velocity, on the other hand, is observed to become negative with time as the surge moves upstream, as shown in Fig. 24d. For the reflected positive waves, the mean velocity is observed to increase towards the obstacle and decrease past the obstacle, see Fig. 24e, f, respectively. Moreover, the mean velocity decreases for each wave after the other. The negative waves behind the obstacle are observed to be slower than the corresponding positive waves. This is in agreement with the theoretical conclusion drawn in [49,50] and references therein, where the front propagating speed $\sqrt{gh}$ of positive waves was approximated to be twice that of negative waves. Additionally, a bore shape (like a downfall) on the velocity profile, opposite of the upsurge on the elevation profile, is observed around the obstacle, which indicates a decrease in velocity around the obstacle due to the obstacle.

Figure 25 shows hydrographs for Points A, B, and C, defined in Fig 22. A series of waves passing through each point is observed traveling on the free-surface as seen in Fig. 25 (a). Waves through Points A and B are bigger compared to those through Point C, which is located downstream of the topography. Also, the waves are seen to reduce in amplitude, one after the other, as they travel away from the source due to the decrease in wave energy.

Moreover, the highest free-surface elevation is registered at Point A and the lowest at Point C. This is due to the blocking effects of the obstacle. However, as the fluid passes over the obstacle, the elevation is observed to grow in time at Point C as it decreases at Points A and B. For Points A and B, elevation tends to decrease towards a unique height equal to the obstacle height.

The mean velocity, on the other hand, is highest at Point C and lowest at Point B, for the first wave, highest at Point B and lowest at Point A for all other subsequent waves. The fluid layer downstream of the obstacle will be very thin, and therefore, to maintain the flow rate, the velocity will be relatively higher. The first wave creates an overflow, which leads to a high velocity at Point C downstream of the obstacle. Subsequent waves do not overflow as much as the first wave, since they are the reflected waves that travel back and forth through Points A and C, respectively, as their velocity reduces in time due to energy loss. For all the subsequent waves, the maximum velocities are registered at Point B. This is due to the fact that the fluid depth is lowest at this point, which means the averaged velocity will need to be highest in order to maintain the flow rate.

The Froude numbers for the first wave are above unity at the three points, hence supercritical, see Fig. 26a. This, however, transcends to subcritical with time for other waves. Moreover, the peak values are larger at
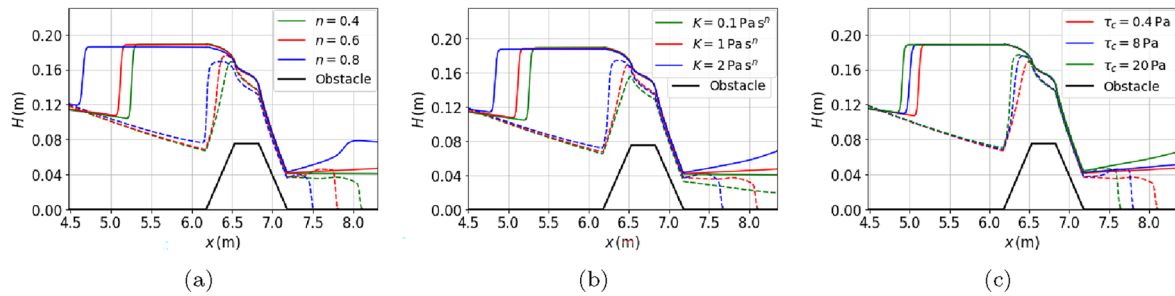
Fig. 27 Effects of rheological parameters on the development of the surge at $t = 2$ s (broken line) and $t = 5$ s (solid line)

Point B compared to A and C, which indicates that the effects of inertia compared to gravity are larger at Point B than at the other two points. The Reynolds numbers, on the other hand, indicate that the flow is laminar, as shown in Fig. 26b. Both the Froude and Reynolds numbers decrease with time, which means that the flow speed is reducing as expected. For the Bingham number in Fig. 26c, the peak values are larger at Point A compared to B and C, and in fact larger than unity, which implies that the yield stress is larger than the viscous stress at point A. Moreover, the Bingham numbers tend to increase with time (wave by wave) at Points A and C but decrease at Point B. This implies that, compared to the yield stress, the shear stresses are reducing at Points A and C, and increasing at Point B.

3.3.2 Effects of rheological parameters

Increasing any of the three rheological parameters is observed to increase the size of the surge, see Fig. 27. Interestingly, as the front position (and speed) of the first wave decreases due to the increase of the rheological parameters (as seen in the previous subsections), the development of the surge upstream of the obstacle is observed to increase. Increasing any of the rheological parameters is observed to reduce the advancement (propagating speed) of the front position of the positive waves but increase the propagation of the corresponding negative waves. This is the conservation of wave energy phenomenon between the negative and positive waves. Further analyses of the effects of the rheological parameters on the flow height and speed at Points A, B, and C of the obstacle, see Fig. 22, are presented in Appendix A.2.

4 Conclusion

Numerical simulations of open-channel dam-break flows for Herschel–Bulkley fluids (like lava, typically of Re < 1000) using SWE over complex topographies are presented. The effects of rheological properties, bed slopes, and fluid depth ratios on the progression speed and height over a dry and wet bed are analyzed. A dam-break flow over a non-flat topography is also discussed. The computed results are compared with experimental results from the literature and are in good agreement. The main conclusions are as follows:

- The front position of the free-surface is observed to advance faster with the decrease of any of the three rheological parameters (K, τ_c, and n), for both dry and wet bed conditions. This is due to the decrease in the friction term that speeds up the fluid evolution when any of these parameters are decreased. The maximum height and velocity at each position are also observed to increase with the decrease of any of these parameters. The thickness at each position, however, increases gradually for the larger values of these parameters, and rapidly within a short period of time for the smaller values. Consequently, two main types of hydrographs are defined: Type I, characterizing rapid flows with an overshoot, and Type II, representing gradual flows. The arrival time of the peak height and velocity is much earlier for Type I than for Type II. Generally, Type I flows are supercritical, especially during the early times of dam-break, before they transcend to subcritical with time, while Type II flows are purely subcritical.
- Shear-thickening fluids are observed to be slower than shear-thinning fluids. Under the same conditions (Re < 1000), power-law fluids appear to spread faster than Herschel–Bulkley, Newtonian, and Bingham fluids in that order. This is mainly due to the effect of the flow-behaviour index, which, when reduced, increases the flow rate. In addition, the power-law and Herschel–Bulkley fluids appear to have a similar flow response, which is different from that of the Newtonian and Bingham fluids. This difference in flow

response is observed to decrease as the power-law index approaches unity, which would correspond to the Newtonian (or Bingham) case. Based on the parametric sensitivity analysis, the power-law index appears to be the dominant factor in dictating the fluid response.

- By increasing the bed slope or the depth ratio, the wave-frontal position moves faster downstream. This is due to the decrease in the rate of viscous dissipation as the downstream fluid level increases. Due to high viscosity, increasing the downstream fluid depth reduces the local Reynolds numbers and hence the interaction between the upstream and downstream fluids, thus reducing the viscous dissipation effects. This is contrary to the observations made in the literature (also observed in the current results) for high Reynolds number flows (in particular, Newtonian flows with a viscosity of water, $K \approx 0.001$Pa s), where the increase of the fluid depth in the downstream region increases the blockage effects (resistance to motion) [25], and hence more energy dissipation, making the front positions tend to decrease.

- The presence of an obstacle is observed to impact the fluid flow speed and height due to its blockage. It causes the formation of an upsurge that develops into a series of negative and positive waves, which propagate upstream and downstream of the obstacle, respectively. Interestingly, increasing any of the rheological parameters is observed to increase the development of the surge upstream of the obstacle but decrease the progression of the front position downstream of the obstacle. This is due to the conservation of momentum between the negative and positive waves.

The present numerical investigations of model sensitivities, based on the SWE model derived in [38], contribute to the understanding of geophysical flows of non-Newtonian fluids over non-flat, dry, and wet beds for hazard assessment and management plans. The future work will be to extend this study to the flow impacts of viscoplastic fluids on a downstream wall and around occlusions.

Availability of data and materials Any data or material presented in this work is available from the corresponding author on request.

Declarations

Conflict of interest The authors have no known conflict of interest to declare.

Ethical approval Not applicable.

A Appendix

A.1 Hydrographs at different positions

To investigate the trend of results at different hydrograph positions, the stage and Froude number (Fr) hydrographs taken at different positions: $x = 1.1$ m, $x = 1.3$ m, and $x = 1.5$ m, respectively, are shown in Fig. 28. Similar stage hydrograph results are observed at the three positions for each value of the rheological parameter n, as shown in Fig. 28a–c. The difference is in the fluid level, which reduces as the fluid flows downstream. This shows that similar hydrograph results are observed at other positions downstream, away from the dam-gate. However, very near the gate, the unsteady flow patterns resulting from the sudden lifting of the gate are not studied in this paper.
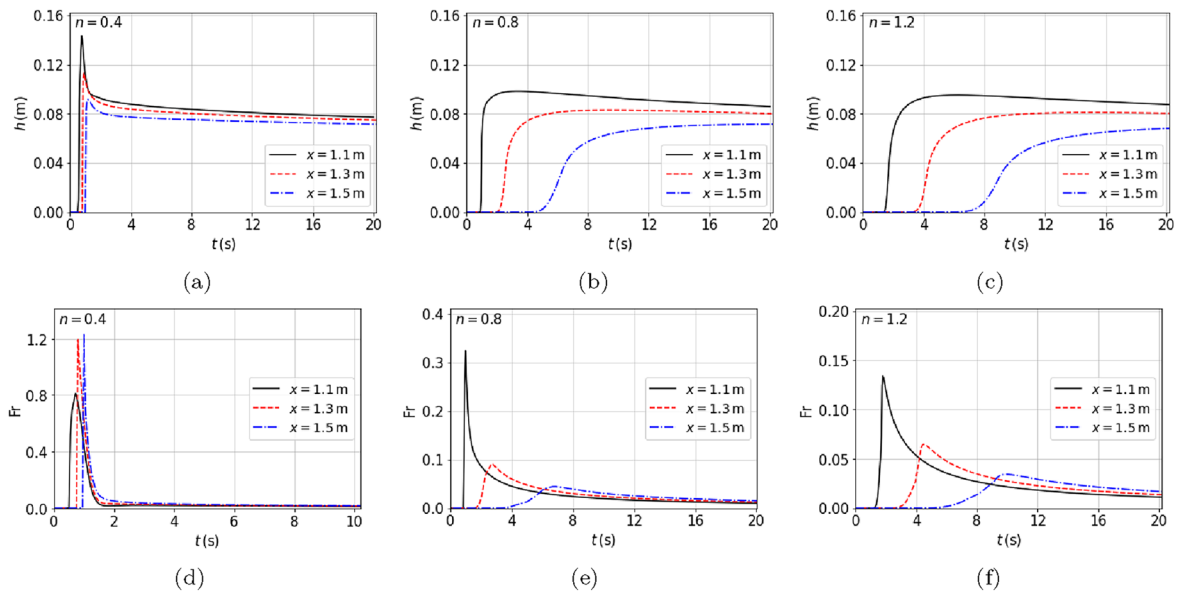
Fig. 28 Stage and Froude number hydrographs at different positions for $n = 0.4$, $n = 0.8$, and $n = 1.2$, respectively. The reference rheological parameters are given by Eq. (3.1)

Likewise, hydrographs of the Froude numbers show similar results at the three positions for each value of the power-law index, see Fig. 28d–f. For the larger n values, the flow is subcritical and the Froude number reduces as the fluid flows downstream, see Fig. 28e, f. However, for $n = 0.4$, the effects of the sudden change in height due to the dam-break are still observed on the Froude number profiles at the three positions. Nevertheless, the flow is supercritical, see Fig. 28a showing the flow changing from subcritical to supercritical. Increasing the power-law index is observed to reduce the Froude number. As mentioned in the previous section, increasing the power-law index increases the basal friction term, which in this case reduces the inertial forces over gravitational forces.

A.2 Effects of rheological parameters over an obstacle

To investigate the effects of rheological parameters further (for Case 3), we study the flow behaviour around Point A ($x = 6.18$ m) upstream of the obstacle, B ($x = 6.68$ m) at the top of the obstacle, and C ($x = 7.18$ m) downstream of the obstacle, as shown in Fig. 22. The effects of K, n, and τ_c on the fluid elevation and on the corresponding mean velocity at each point are shown in Figs. 29, 30, and 31, respectively. Increasing any of the three parameters is observed to increase the maximum height at Points B and C, and decrease the maximum height at Point A. This is due to the formation of the surge upstream of Point A, which increases as any of the three rheological parameters is increased, resulting in a decrease in the fluid height. Again, this is the result of the energy-balancing phenomenon between waves moving backward and those moving forward.
However, by increasing any of these parameters, the mean velocity is observed to decrease at the three points. Velocity at Point A drops drastically within a short period of time due to the blockage effects of the obstacle. In particular, Point A records the highest fluid height and the lowest velocity, while Point C records the lowest height but the highest velocity, an indication that the flow tries to maintain the flow rate.
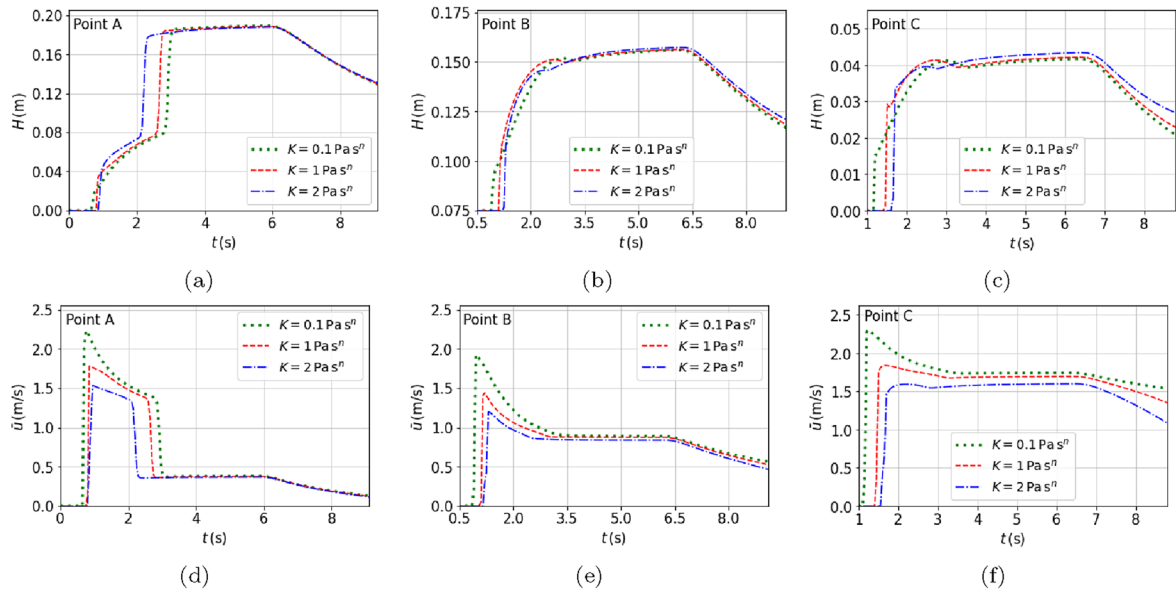
Fig. 29 Effects of consistency index: hydrographs for the **a–c** fluid elevations, and **d–f** corresponding mean velocities at Points A, B, and C, respectively
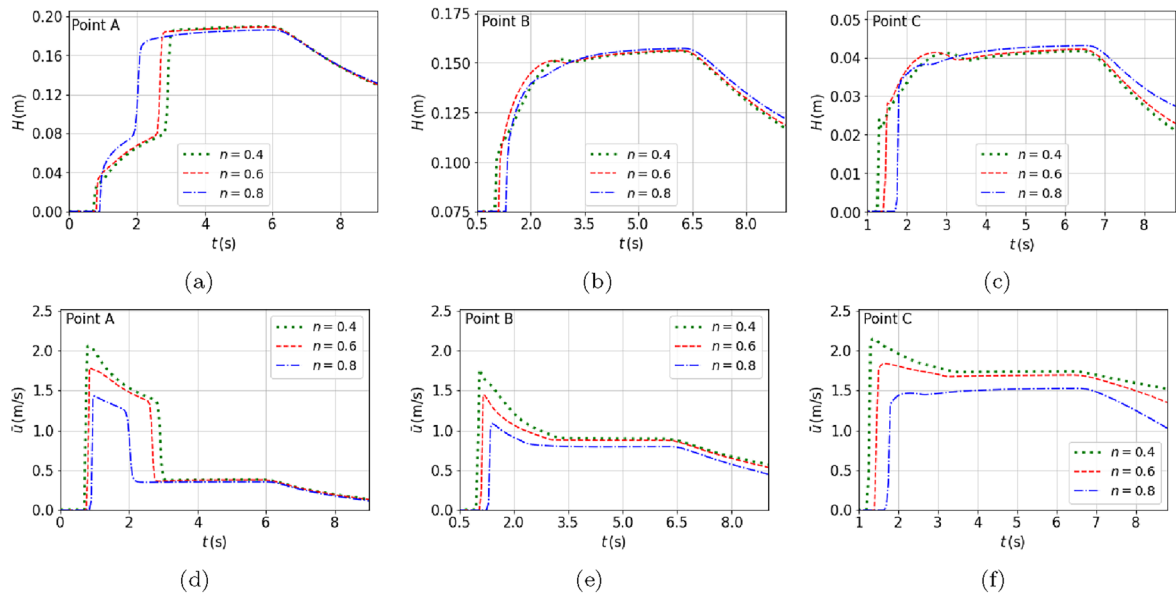

Fig. 30 Effects of power-law index: hydrographs for the **a–c** fluid elevations, and **d–f** corresponding mean velocities at Points A, B, and C, respectively
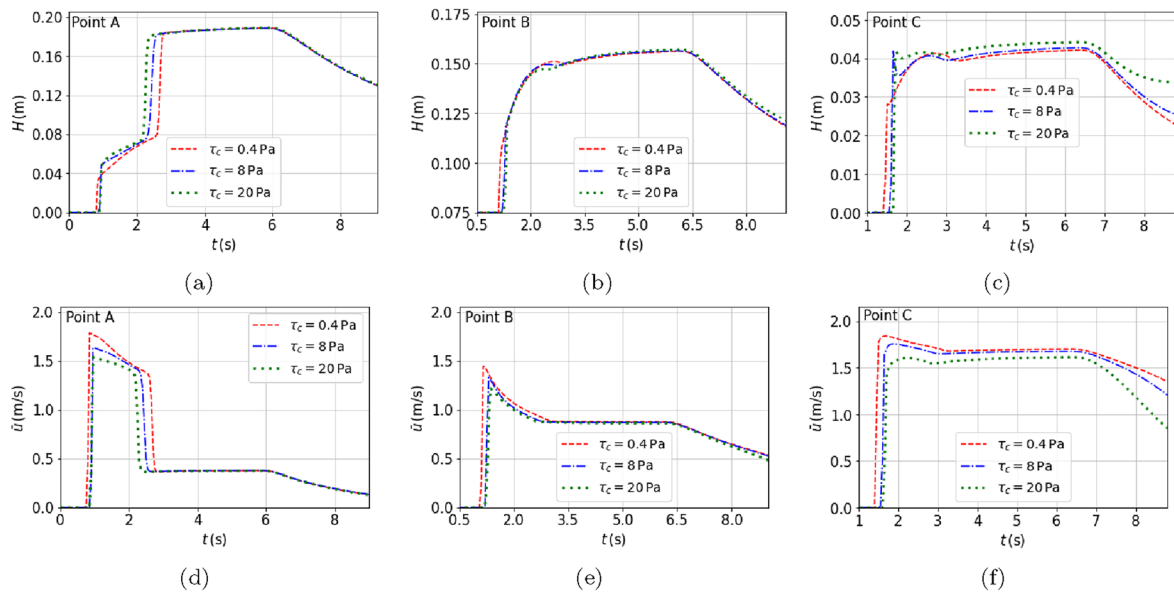
Fig. 31 Effects of yield stress: hydrographs for the **a**– **c** fluid elevations and **d**–**f** corresponding averaged velocities at Points A, B, and C, respectively

References

1. Huang, X., Garcia, M.H.: A Herschel–Bulkley model for mud flow down a slope. J. Fluid Mech. **374**, 305–333 (1998)
2. Ancey, C.: Plasticity and geophysical flows: a review. J. Non-Newton. Fluid Mech. **142**, 4–35 (2007)
3. Hogg, A.J., Matson, G.P.: Slumps of viscoplastic fluids on slopes. J. Non-Newton. Fluid Mech. **158**(1–3), 101–112 (2009)
4. Balmforth, N.J., Frigaard, I.A., Ovarlez, G.: Yielding to stress: recent developments in viscoplastic fluid mechanics. Annu. Rev. Fluid Mech. **46**, 121–146 (2014)
5. Frigaard, I.: Simple yield stress fluids. Curr. Opin. Colloid Interface Sci. **43**, 80–93 (2019)
6. Walder, J.S., O'Connor, J.E.: Methods for predicting peak discharge of floods caused by failure of natural and constructed earthen dams. Water Resour. Res. **33**(10), 2337–2348 (1997)
7. Papale, P.: Rational volcanic hazard forecasts and the use of volcanic alert levels. J. Appl. Volcanol. **6**(1), 1–13 (2017)
8. Merz, B., Kuhlicke, C., Kunz, M., Pittore, M., Babeyko, A., Bresch, D.N., Domeisen, D.I.V., Feser, F., Koszalka, I., Kreibich, H.: Impact forecasting to support emergency management of natural hazards. Rev. Geophys. **58**(4), e2020RG000704 (2020)
9. Griffiths, R.W.: The dynamics of lava flows. Annu. Rev. Fluid Mech. **32**, 477–518 (2000)
10. Khoshkonesh, A., Nsom, B., Gohari, S., Banejad, H.: A comprehensive study on dam-break flow over dry and wet beds. Ocean Eng. **188**, 106279 (2019)
11. Cochard, S.: Measurements of time-dependent free-surface viscoplastic flows down steep slopes. Technical report, EPFL (2007)
12. Liu, W., Wang, B., Guo, Y., Zhang, J., Chen, Y.: Experimental investigation on the effects of bed slope and tailwater on dam-break flows. J. Hydrol. **590**, 125256 (2020)
13. Ozmen-Cagatay, H., Kocaman, S.: Dam-break flow in the presence of obstacle: experiment and CFD simulation. Eng. Appl. Comput. Fluid Mech. **5**, 541–552 (2011)
14. Chanson, H., Jarny, S., Coussot, P.: Dam break wave of thixotropic fluid. J. Hydraul. Eng. **132**(3), 280–293 (2006)
15. Hulme, G.: The interpretation of lava flow morphology. Geophys. J. Int. **39**(2), 361–383 (1974)
16. Moyers-Gonzalez, M., Hewett, J.N., Cusack, D.R., Kennedy, B.M., Sellier, M.: Non-isothermal thin-film flow of a viscoplastic material over topography: critical Bingham number for a partial slump. Theor. Comput. Fluid Dyn., pp. 1–22 (2023)
17. Bird, R.B., Dai, G.C., Yarusso, B.J.: The rheology and flow of viscoplastic materials. Rev. Chem. Eng. **1**(1), 1–70 (1983)
18. Saramito, P., Wachs, A.: Progress in numerical simulation of yield stress fluid flows. Rheol. Acta **56**, 211–230 (2017)
19. Balmforth, N.J., Craster, R.V.: A consistent thin-layer theory for Bingham plastics. J. Non-Newton. Fluid Mech. **84**, 65–81 (1999)
20. Balmforth, N.J., Craster, R.V., Perona, P., Rust, A.C., Sassi, R.: Viscoplastic dam breaks and the Bostwick consistometer. J. Non-Newton. Fluid Mech. **142**(1–3), 63–78 (2007)
21. Matson, G.P., Hogg, A.J.: Two-dimensional dam break flows of Herschel–Bulkley fluids: the approach to the arrested state. J. Non-Newtonian Fluid Mech. **142**(1–3), 79–94 (2007)
22. Minussi, R.B., Maciel, G.D.F.: Numerical experimental comparison of dam break flows with non-Newtonian fluids. J. Braz. Soc. Mech. Sci. Eng. **34**, 167–178 (2012)
23. Ancey, C., Cochard, S.: The dam-break problem for Herschel–Bulkley viscoplastic fluids down steep flumes. J. Non-Newton. Fluid Mech. **158**, 18–35 (2009)
24. Cochard, S., Ancey, C.: Experimental investigation of the spreading of viscoplastic fluids on inclined planes. J. Non-Newton. Fluid Mech. **158**, 73–84 (2009)

25. Zhang, F., Wang, B., Guo, Y.: Experimental study of the dam-break waves in triangular channels with a sloped wet bed. Ocean Eng. **255**, 111399 (2022)
26. Hunt, B.: Asymptotic solution for dam-break on sloping channel. J. Hydraul. Eng. **109**(12), 1698–1706 (1983)
27. Ozmen-Cagatay, H., Kocaman, S., Guzel, H.: Investigation of dam-break flood waves in a dry channel with a hump. J. Hydro-environ. Res. **8**(3), 304–315 (2014)
28. Aureli, F., Maranzoni, A., Mignosa, P., Ziveri, C.: Dam-break flows: acquisition of experimental data through an imaging technique and 2D numerical modeling. J. Hydraul. Eng. **134**(8), 1089–1101 (2008)
29. Liang, Q., Marche, F.: Numerical resolution of well-balanced shallow water equations with complex source terms. Adv. Water Resour. **32**, 873–884 (2009)
30. Bernabeu, N., Saramito, P., Smutek, C.: Numerical modelling of non-Newtonian viscoplastic flows: part II. viscoplastic fluids and general tridimensional topographies. Int. J. Numer. Anal. Model. **11**, 213–228 (2014)
31. Acary-Robert, C., Fernández-Nieto, E.D., Narbona-Reina, G., Vigneaux, P.: A well-balanced finite volume-augmented Lagrangian method for an integrated Herschel–Bulkley model. J. Sci. Comput. **53**, 608–641 (2012)
32. Balmforth, N.J., Craster, R.V., Rust, A.C., Sassi, R.: Viscoplastic flow over an inclined surface. J. Non-Newton. Fluid Mech. **139**, 103–127 (2006)
33. Chambon, G., Ghemmour, A., Laigle, D.: Gravity-driven surges of a viscoplastic fluid: an experimental study. J. Non-Newton. Fluid Mech. **158**(1–3), 54–62 (2009)
34. Muchiri, D.K., Cusack, D.R., Hewett, J.N., Sellier, M., Moyers-Gonzalez, M., Monnier, J.: Identification of rheological parameters for shallow water flows of viscoplastic fluids using elevation hydrographs. Phys. Fluids **36**(1) (2024)
35. Fernández-Nieto, E.D., Noble, P., Vila, J.-P.: Shallow water equations for non-Newtonian fluids. J. Non-Newton. Fluid Mech. **165**, 712–732 (2010)
36. Boutounet, M., Monnier, J., Vila, J.-P.: Multi-regime shallow free surface laminar flow models for quasi-Newtonian fluids. Eur. J. Mech.-B/Fluids **55**, 182–206 (2016)
37. Conroy, C.J., Lev, E.: A discontinuous Galerkin finite-element model for fast channelized lava flows v1. 0. Geosci. Model Dev. **14**(6), 3553–3575 (2021)
38. Muchiri, D.K., Monnier, J., Sellier, M.: Derivation and numerical resolution of 2D shallow water equations for multi-regime flows of Herschel–Bulkley fluids. Eur. J. Mech.-B/Fluids, Under revision https://hal.science/hal-03968946/ (2024)
39. Denisenko, D., Richard, G., Chambon, G.: A consistent three-equation shallow-flow model for Bingham fluids. J. Nonnewton. Fluid Mech. **321**, 105111 (2023)
40. Chambon, G.: Quelques contributions à la modélisation des écoulements à surface libre de fluides complexes. Ph.D. thesis, HDR en Sciences de la Planète et de l'Environnement, Université de Grenoble I (2014)
41. Fernández-Nieto, E.D., Garres-Díaz, J., Vigneaux, P.: Multilayer models for hydrostatic Herschel–Bulkley viscoplastic flows. Comput. Math. Appl. **139**, 99–117 (2023)
42. Chaudhry, M.H.: Open-Channel Flow, vol. 523. Springer (2008)
43. Rohatgi, A.: WebPlotDigitizer (2024). https://automeris.io/WebPlotDigitizer.html
44. Ramírez, J.A.: Prediction and modeling of flood hydrology and hydraulics. Inland Flood Hazards: Human, Riparian and Aquatic Communities, p. 498 (2000)
45. Lane, S.N., Landström, C., Whatmore, S.J.: Imagining flood futures: risk assessment and management in practice. Philos. Trans. R. Soc. A: Math. Phys. Eng. Sci. **369**(1942), 1784–1806 (2011)
46. Turhan, E., Özmen-Çağatay, H., Kocaman, S.: Experimental and numerical investigation of shock wave propagation due to dam-break over a wet channel. Pol. J. Environ. Stud. **28**, 2877–2898 (2019)
47. Blatt, H., Tracy, R., Owens, B.: Petrology: Igneous, Sedimentary, and Metamorphic. Macmillan (2006)
48. Chevrel, M.O., Pinkerton, H., Harris, A.J.L.: Measuring the viscosity of lava in the field: a review. Earth Sci. Rev. **196**, 102852 (2019)
49. Castro-Orgaz, O., Chanson, H.: Ritter's dry-bed dam-break flows: positive and negative wave dynamics. Environ. Fluid Mech. **17**, 665–694 (2017)
50. Yang, S., Yang, W., Qin, S., Li, Q.: Comparative study on calculation methods of dam-break wave. J. Hydraul. Res. (2018)